J Neurophysiol 121: 2341–2357, 2019.
First published April 10, 2019; doi:10.1152/jn.00738.2018.

RESEARCH ARTICLE | *Cellular and Molecular Properties of Neurons*

Autonomous patch-clamp robot for functional characterization of neurons in vivo: development and application to mouse visual cortex

Gregory L. Holst,[1] William Stoy,[2] Bo Yang,[1] Ilya Kolb,[2] Suhasa B. Kodandaramaiah,[3] Lu Li,[4] Ulf Knoblich,[4] Hongkui Zeng,[4] Bilal Haider,[2] Edward S. Boyden,[5,6,7] and Craig R. Forest[1]

[1]*George W. Woodruff School of Mechanical Engineering, Georgia Institute of Technology, Atlanta, Georgia;* [2]*Wallace H. Coulter Department of Biomedical Engineering, Georgia Institute of Technology, Atlanta, Georgia;* [3]*Department of Mechanical Engineering, University of Minnesota, Minneapolis, Minnesota;* [4]*Allen Institute for Brain Science, Seattle, Washington;* [5]*Media Arts and Sciences, Massachusetts Institute of Technology, Cambridge, Massachusetts;* [6]*McGovern Institute, Massachusetts Institute of Technology, Cambridge, Massachusetts; and* [7]*Koch Institute, Massachusetts Institute of Technology, Cambridge, Massachusetts*

Submitted 30 October 2018; accepted in final form 12 March 2019

Holst GL, Stoy W, Yang B, Kolb I, Kodandaramaiah SB, Li L, Knoblich U, Zeng H, Haider B, Boyden ES, Forest CR. Autonomous patch-clamp robot for functional characterization of neurons in vivo: development and application to mouse visual cortex. *J Neurophysiol* 121: 2341–2357, 2019. First published April 10, 2019; doi: 10.1152/jn.00738.2018.—Patch clamping is the gold standard measurement technique for cell-type characterization in vivo, but it has low throughput, is difficult to scale, and requires highly skilled operation. We developed an autonomous robot that can acquire multiple consecutive patch-clamp recordings in vivo. In practice, 40 pipettes loaded into a carousel are sequentially filled and inserted into the brain, localized to a cell, used for patch clamping, and disposed. Automated visual stimulation and electrophysiology software enables functional cell-type classification of whole cell-patched cells, as we show for 37 cells in the anesthetized mouse in visual cortex (V1) layer 5. We achieved 9% yield, with 5.3 min per attempt over hundreds of trials. The highly variable and low-yield nature of in vivo patch-clamp recordings will benefit from such a standardized, automated, quantitative approach, allowing development of optimal algorithms and enabling scaling required for large-scale studies and integration with complementary techniques.

NEW & NOTEWORTHY In vivo patch-clamp is the gold standard for intracellular recordings, but it is a very manual and highly skilled technique. The robot in this work demonstrates the most automated in vivo patch-clamp experiment to date, by enabling production of multiple, serial intracellular recordings without human intervention. The robot automates pipette filling, wire threading, pipette positioning, neuron hunting, break-in, delivering sensory stimulus, and recording quality control, enabling in vivo cell-type characterization.

automated; layer 5; in vivo; patch clamp; robotic; visual cortex

INTRODUCTION

Much work in neuroscience is aimed at revealing how different cell types, defined by their electrophysiology, morphology, or gene expression, respond to inputs and work together in circuits to implement brain computations, as well as what role different cell types play in brain disorders. There remains no unified taxonomy of cell types, nor a simple methodology for evaluating cell types present in a given brain circuit, despite outstanding recent efforts (Cadwell et al. 2016; Tasic et al. 2017). Patch-clamp recording (Sakmann and Neher 1984), while something of an art form, is the gold standard technique for cell-type classification, enabling the measurement of transmembrane voltages, intracellular currents, and the study of functional responses in electrically excitable cells in vivo.

Previously, whole cell-patch clamping has been used in the visual cortex to establish a link between functional electrophysiology and morphology of cell types in layer 6 (L6) (Vélez-Fort et al. 2014). In an extraordinary effort, the team characterized the intracellular electrophysiology and function of 80 neurons in vivo and coupled electrophysiology and morphology, including projections, on a subset of 16 cells. Layer 5 (L5) in the primary visual cortex (V1) has also been of great interest; it functions as an output layer from the cortex to subcortical areas (Bourassa and Deschênes 1995; Hallman et al. 1988; Hattox and Nelson 2007; Hübener and Bolz 1988; Hübener et al. 1990; Kasper et al. 1994; Kim et al. 2015; Tsiola et al. 2003; Zarrinpar and Callaway 2016) and higher visual areas (Kim et al. 2015; Lur et al. 2016).

In prior work, we discovered that "blind" in vivo whole cell patching of neurons, could be reduced to a reliable algorithm, and the whole cell state could be established in >40% of detected cells on average (Kodandaramaiah et al. 2012). This device, which we termed the autopatcher, automates the pressure, position, and electrical control of the pipette for a single recording attempt. For large, systematic cell-type studies, however, ideally, one would enable the autopatcher to work continuously and autonomously by reducing the need for the operator to exchange pipettes, deliver physiological stimuli, and monitor and adjust parameters to maintain the health of the whole cell recording. Here, we show the development of a robotic system to autonomously acquire multiple consecutive patch-clamp recordings in vivo and use this novel tool to

Address for reprint requests and other correspondence: C. R. Forest, George W. Woodruff School of Mechanical Engineering, Georgia Institute of Technology, Atlanta GA 30332 (e-mail: cforest@gatech.edu).

investigate bursting (Shai et al. 2015), back-propagating action potentials (Larkum et al. 1999), plateau potentials, and visual response (Kim et al. 2015; Lur et al. 2016) in L5 visual cortex. This work represents the most fully automated in vivo intracellular electrophysiology experiment to date. We demonstrate the methodology in mouse V1 L5 to validate the quality of the recordings, throughput, and cell characterization in L5.

MATERIALS AND METHODS

We performed in vivo patch-clamp recordings in 8–14-wk-old C57BL/6 male mice (Charles River Laboratories International) anesthetized under 0.75–1.2% isoflurane in pure oxygen (see Fig. 1 for the steps in a typical patch-clamp experiment). All experimental procedures were performed in accordance with approved protocols under the supervision of the Institutional Animal Care and Use Committee of the Georgia Tech Institute of Technology and Allen Institute for Brain Science. Intracellular solution contains 135 mM potassium gluconate, 10 mM HEPES, 4 mM potassium chloride, and 1 mM EGTA dissolved in deionized H_2O with the pH adjusted to 7.30 using 1-μl additions of 8 N KOH being careful to wipe down the exterior of the pipette tip for more accurate additions. This stock solution is first prepared in a 50-ml batch, aliquoted into 4-ml volumes in 5-ml cryogenic vials (no. 3015; Globe Scientific, Mahwah, NJ), and stored at −50°C. Eight milliliters of stock solution were thawed as needed, and 0.3 mM GTP-Na, 5 mM ATP-Mg, and 10 mM Na_2-phosphocreatine were added. The pH is then readjusted using 8 N KOH to 7.25 and aliquoted into 32, 0.5-ml centrifuge tubes (Eppendorf 022363611) (250 μl in each), stored at −50°C, and used within 6 mo.

Surgical Preparation

The surgical preparation consists of implanting a titanium headplate on the skull of the mouse to increase the stability of the recordings. First, anesthesia is induced using 5% isoflurane in 100% oxygen followed by 1.1–1.5% for maintenance during surgery. The skull of the animal is positioned in a stereotax (Kopf 963, 923-B, 922; Kopf Instruments, Tujunga, CA) using nonrupture ear bars. Ophthalmic ointment (Puralube) is applied to the eyes to prevent the formation of cataracts. Subcutaneous meloxicam (0.2–1.0 mg/kg), atropine (0.05 mg/kg), and buprenorphine (0.05–0.1 mg/kg) are administered after induction. Meloxicam and buprenorphine help reduce brain swelling and variability between animals by reducing inflammation and reducing the sympathetic response. Optionally, dexamethasone (3.2 mg/kg) can be administered ideally between 8 and 12 h before surgery (can be given a minimum of 2 h before) to help reduce brain swelling. Atropine helps reduce airway secretions and reduces gasping, especially during long experiments (>1 h under anesthesia).

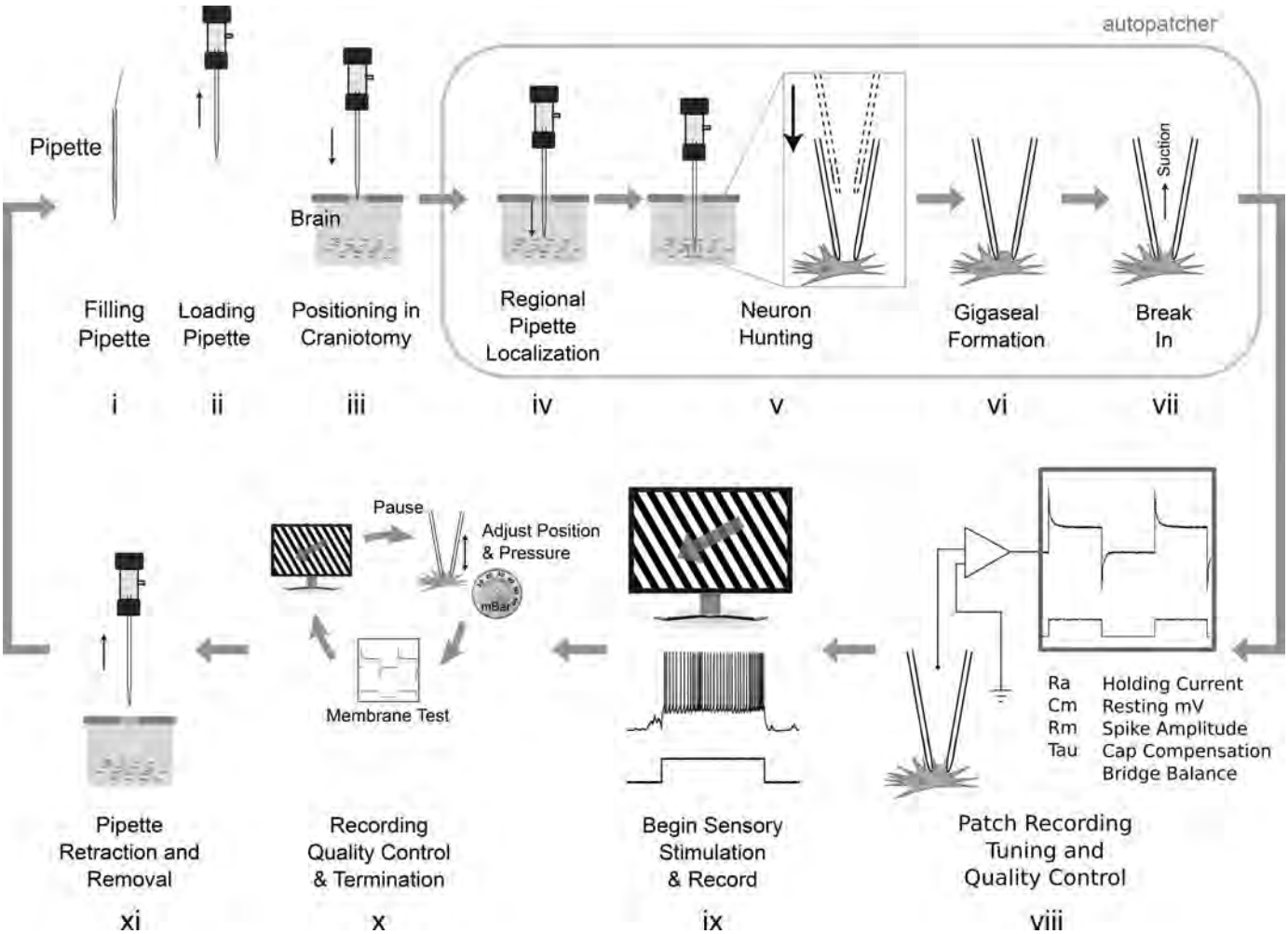

Fig. 1. *i–xi*: steps in a typical patch-clamp experiment. *Steps iv–vi* were automated previously (Kodandaramaiah et al. 2012, 2016). The autonomous robot in this work automatically performs *steps i–xi* and obtains multiple consecutive recordings completely without human interaction (gray arrow). Each recording attempt requires 5.5 min, not including *steps viii–x*.

Once the animal is positioned in the stereotax, a midline incision is made along the scalp using a no. 10 scalpel, and a small portion of the skin is removed to expose the top of the skull (~8–10 mm in diameter). The residual fascia and periostium should be removed to allow good adhesion between the dental cement and the skull. The muscle connections on the lateral and posterior edges are detached and retracted 1 mm using a no. 11 scalpel. The muscle is affixed using surgical adhesive (e.g., Vetbond) to expose the corner transition between the top and sides of the skull. The skull is then leveled with respect to lambda and bregma using the stereotax, and the titanium head post (Fig. 2, *A* and *B*) is placed on the surface of the skull. The inner apical edge of the 11.5-mm diameter opening in the headplate should be positioned ~1.25 mm anterior to bregma and centered laterally. Dental cement (Metabond Parkell, S371, S398, S396, S387) is applied on the underside and vertical edges of the headplate around the periphery of the opening and around the entire perimeter near the skull (Fig. 2*C*). This surgical technique was developed by the Allen Institute for Brain Science.

Two craniotomies are made at 1.25 mm anterior and 2.25 mm lateral to lambda in both hemispheres. A high-speed dental drill (ECO450, 1/8″ Collet; American Rotary Tools Company, Monrovia, CA), with a 250-μm diameter square end mill, is attached to a three-axis manipulator to allow precise control of the drilling location and depth. After locating the end mill above the desired location on the skull, the manipulator lowers the drill 190 μm from the surface of the skull to drill a precise craniotomy. This technique is based on the automated craniotomy robot but operates without using the electrical feedback (Pak et al. 2015). Vascularization in the skull above the visual cortex often results in false-positive detections of the brain surface, prematurely stopping the drill. After the initial drilling using the manipulator, a dental drill (3/32″ collet) with a spherical dental bur (diameter 250 μm, no. 1/4 size) is used to manually countersink the area around the drilling location. The tip of a 29 gauge needle (ExcelInt 26018) is then used to lift the bone island remaining in the drilling location. If not completely detached, additional manual countersinking around the periphery and mechanical separation using the needle can separate the island. Extreme care should be taken to avoid damaging the surface of the brain when removing the bone. The opening in the skull should be as small as possible (200–350 μm) while exposing sufficient tissue to allow pipette insertion without damaging blood vessels or contacting the dura. The dura is retracted by delicately rubbing the dura using the tip of fine (not ultra-fine) tweezers that are sufficiently rounded to avoid damaging the cortex. Alternatively, the tip of a 29-gauge needle that has been bent so that the tip points parallel to the surface of the cortex can be used to cut a slit in the dura and fold it to either side of the slit. Some groups leave the dura intact to avoid damaging the cortex, but we have found that this increases the rate of clogged pipettes (Desai et al. 2015).

Throughout the surgical procedure, the surface of the brain and dura is kept moist by submersing it in ACSF or 0.9% saline once the bone is removed. While the dura is being manipulated, however, it is most easily visualized and removed after the fluid has been wicked away. Care should be taken to periodically hydrate the surface of the brain during this procedure if it begins to dry (every 1–2 min). Bleeding can be controlled by irrigating with ACSF or 0.9% saline and utilizing absorbent spears (Sugi; Kettenbach, Eschenburg, Germany). With careful manipulation of the dura, bleeding can occasionally be avoided altogether. Clotting on the surface of the brain should be avoided, as it increases the incidence of clogged pipettes, even after the clots are removed. Throughout the remainder of the experiment, the surface of the brain should be covered by ACSF or 0.9% saline, except when positioning the tip of the pipette above the surface of the brain. If pipette clogging is problematic, several cycles of irrigation and drying will help remove debris from the area surrounding the craniotomy. Filtering the ACSF or 0.9% saline can also reduce clogging. The entire surgical procedure requires 45–90 min. Additional information on our surgical and experimental methods is detailed in (Kodandaramaiah et al. 2016).

After surgery, the animal was relocated to the electrophysiological apparatus, in which the headplate is secured horizontally using aluminum optical filter clamps (Eskma Optics, 830–0055) and 12-mm optical posts. Isoflurane (0.75–1.1%) in 100% oxygen is continued throughout the experiment. The level of anesthesia was carefully regulated as to just suppress the toe pinch reflex. Any additional anesthesia will unnecessarily suppress additional cortical activity. The temperature of the animal was maintained at 37°C, using a low-noise warming pad (FHC, DC temperature controller FHC40908, small heating pad FHC-4090207). If the animal is too cold, the breathing will slow, and gasping will become more evident. Motion of the spinal cord during gasping causes severe motion artifacts and will effectively prevent gigaseal formation if not addressed. The posture of the mouse should be adjusted to reduce this motion by positioning the head of the mouse ~22 mm above the warming pad (Fee 2000). The breathing rate should be at least 0.5 Hz.

The ophthalmic ointment is removed from the eyes before beginning the recordings and hyaluronan eye drops and contact lenses (Ocuscience, 2.5 mm) were used to help maintain optical clarity and to reduce the formation of cataracts. Euthanasia was performed via anesthetic overdose.

Electrophysiology

To enable recording from either hemisphere, two 609-mm monitors (diagonal measurement) are placed to either side and in front of the animal at a 55° angle measured from a vertically oriented plane intersecting the midline of the animal, and 190 mm from the eye at the closest point. The lower edge of the monitors is placed 100 mm below eye level, so as to cover 74° of visual space in altitude, and 98° in azimuth. Drifting sinusoidal gratings with spatial frequencies 0.01, 0.02, 0.04, and 0.08 are displayed with a fixed 2-Hz temporal frequency. Eight different grating orientations are displayed with a contrast ratio of 0.8. The PsychoPy software suite is used to generate and display the stimulus with slight modifications for dual-monitor display. The visual stimulus is displayed on the monitor contralateral

Fig. 2. Diagram of the head post (*A* and *B*) and dental cement application (*C*). In *C*, bregma and lambda are identified by B and L respectively.

to the hemisphere of the recording, while the other monitor was kept blank. A photodiode (ThorLabs, PDA25K) is placed in front of one monitor to directly record the onset of the stimulus in parallel with the recording. Each combination of spatial frequency and orientation is displayed eight times, in a randomized fashion. Ten seconds of blank stimulus (gray screen) preceded the first stimulus presentation and followed the final presentation. Each stimulus is presented for two seconds, followed by a blank stimulus displayed for 1 s. For every 10 visual stimulus presentations, a 2-s blank stimulus is also presented. These blank stimuli are also included in the randomization scheme.

We used a Multiclamp 700B intracellular amplifier, Digidata 1440 for data acquisition, and pClamp 10 software for processing (Molecular Devices, Sunnyvale, CA). The liquid junction potential between the pipette and the bath is corrected just prior to neuron hunting. The bridge balance was automatically corrected using the algorithm detailed in the following section. The pipette capacitance was compensated in current clamp using 80–90% of the automated compensation value determined by the amplifier just before break in. These compensation steps were performed using the algorithms built-into the Multiclamp Commander amplifier control software. To execute them autonomously, they were triggered by the robot software through the DLL software interface to the amplifier software. Adding functionality to trigger other compensation (e.g., series resistance compensation in voltage clamp) is a straightforward extension of the code that would enable the robot to perform voltage-clamp recordings if desired. The recordings were postprocessed using MATLAB (MathWorks).

We pulled pipettes using 1.5 × 0.86 mm filamented borosilicate capillaries with fire-polished ends (Warner G150–4) using a flaming brown pipette puller (P-97; Sutter Instruments, Novato, CA) with a 3 × 3 mm platinum box filament. The pipettes had an average resistance of 6.5 MΩ (σ = 1.1 MΩ) and ranged from 3.9 to 9 MΩ. We optimized the pipettes to have a wide cone angle at the tip, as described previously (Kodandaramaiah et al. 2016; Stockslager et al. 2016)

Spiking Response

For visual response characterization, we compared the number of spikes per 1-s interval of visual stimulus to the number of spikes during the 1-s blank periods between stimuli (Li et al. 2017). The results were approximately Poisson distributed with some nonideal dispersion where $\mu < \sigma^2$ (ideally $\mu = \sigma^2$ for a true Poisson distribution) and some zero inflation (i.e., results dominated by many 1-s periods with zero spikes). More advanced methods, such as the negative binomial distribution could more effectively account for dispersion and zero inflation at the cost of higher complexity and were unnecessary, given the highly significant differences in these data set (McElduff et al. 2010).

Supplemental Table S2 (available online at https://doi.org/10.6084/m9.figshare.7946504.v2) shows the total spike counts, the number of 1-s intervals analyzed, the *P* values using the rate ratio exact test, the calculated rate ratio (λ_v/λ_b) assuming a perfect Poisson distribution, and a rate ratio calculated from a Poisson regression. We confirmed the validity of the test by dividing the periods of blank stimuli from a single recording into two groups, and the test did not reject the null hypothesis of similarity between the groups. The number of spikes during the visual stimulus is a sum from all of the responses to all orientations and spatial frequencies.

Software

This open-source software is freely available on www.autopatcher.org.

Once a filled pipette is positioned in the automated pipette holder above the surface of the brain, the robot first checks the resistance of the pipette to reject any that do not fall within the optimal 3–9-MΩ range in voltage clamp (VC) (10 mV, 10-Hz square wave, Fig. 3*A*). Then Fig. 3*B* shows the pipette insertion into the brain or regional pipette localization (Fig. 3*B*, arrow) indicated by abrupt change in slope of the current recording, breakage check (first current injection), and clog check (second current injection). If the pipette tip breaks during insertion (e.g., by contact with bone fragments), the first current injection detects a resistance drop within 2 s, and the high positive pressure is immediately released to prevent tissue damage. The pipette is then automatically retracted and replaced.

If the pipette is inserted to the region of interest in the brain successfully, neuron hunting then commences with pipettes moving in 2-μm steps and resistances measured between steps (Fig. 3*C*). A neuron is detected by a drop in the amplitude of the injected square wave over two steps, indicating an increase in resistance (Fig. 3*D*, left arrow). Gigaseal formation is then performed (Fig. 1*vi*) as follows: the motion is halted, 10 resistance measurements are acquired to confirm firm contact with the cell membrane by confirming that the reduced resistance is sustained or further reduced, and the low-positive pressure is released (Fig. 3*D*, right arrow), and gigasealing commences (Kodandaramaiah et al. 2012, 2016). Fifteen seconds after pressure is released, negative pressure (−15 mbar) is applied to enhance seal formation (not shown). After 10 s, negative pressure is released, and the holding voltage is ramped from −30 to −70 mV over 30 s. For additional details on the pipette resistance check, regional pipette localization, neuron hunting, or gigaseal formation (Fig. 1, *iv* and *vi*), see the prior work on autopatching (Kodandaramaiah et al. 2012).

Break-in algorithm. In implementing the algorithms to determine when and how to break into a neuron, we explored alternative strategies to those previously reported. DeWeese (DeWeese 2007) suggests that breaking in immediately is optimal, while others wait 3–5 min for the seal to stabilize (Cadwell et al. 2016). The simplest algorithm is to break in once resistance has reached 1 GΩ (Desai et al. 2015). However, in cases where a cell is sealing quickly and low noise is desired, a higher seal resistance may be obtainable by waiting (>2 GΩ) (Walz 2010).

We developed an algorithm that monitors the stability of the seal using four conditions to balance expediency, while maximizing seal resistance. The first condition requires that at least one resistance measurement >1.2 GΩ is acquired. Additional conditions relate to the rate of change (slope) of the resistance recording, which typically reaches maximum at the onset of gigaseal formation. Resistance measurements are acquired at 1 Hz. Using two moving windows, one with 5 and another with 30 consecutive resistance measurements, a linear fit is performed on the data from both windows to determine the slopes of the resistance recordings. These slope calculations are stored in an array. For break-in to proceed, the most recent 30-point resistance measurements must have a slope that is <50 MΩ/s and <50% of the global maximum slope measured during gigasealing. Lastly, for break-in to proceed, in addition to these conditions, the five most recent resistance measurements must have a slope <1 MΩ/s, thus responding rapidly to resistance stabilization. Once all four conditions are met (>1.2 GΩ, slope <50 MΩ/s <50% of global max slope, and five point slope <1 MΩ/s), the automated pipette capacitive compensation routine is executed and break-in commences.

We developed these conditions using historical gigasealing resistance measurements from 90 trials to test the robustness of different algorithms and whether they matched what an experimenter would do during a manual experiment. Namely, break-in should be performed once the slope has decreased to near plateau (<50 MΩ/s), as compared against maximum slope. Further, manual patching requires a rapid response (5 s at 1 Hz) once the seal has stabilized (<1 MΩ/s). This algorithm, by monitoring the rates of sealing, either matches or is slightly more conservative (waits slightly longer) than a human operator in deciding when to break in.

For cells that seal slowly (>2 min), the second, third, and fourth conditions are ignored and break in is attempted immediately after reaching 1.2 GΩ. These slowly sealing cells failed on break in and never resulted in a successful whole cell recording in our experiments;

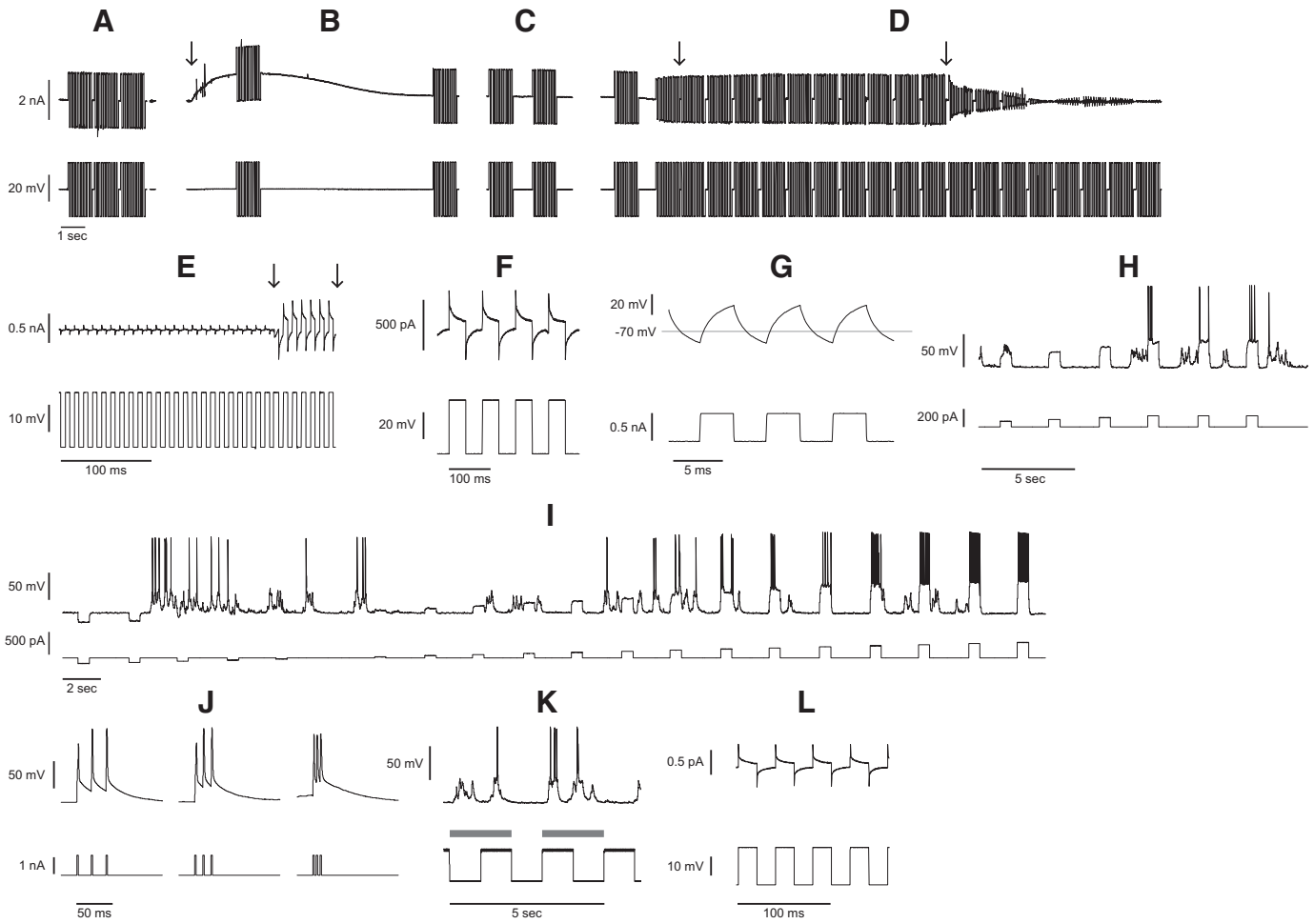

Fig. 3. Algorithmic steps of the autonomous autopatcher. *A*: pipette resistance check. *B*: pipette insertion, breakage check, and clog check. Arrow denotes the moment the pipette is lowered into the brain followed by a tip breakage resistance check. *C*: neuron hunting. *D*: neuron detection and gigasealing. First arrow indicates the moment the last resistance measurement in a monotonically increasing series met the threshold required for neuron detection. Ten resistance measurements are taken to confirm the resistance does not decrease, and then the second arrow denotes low positive pressure release. *E*: feedback-controlled break-in. First arrow denotes the moment of break-in. Second arrow denotes the moment that the negative pressure ramp was released. *F*: membrane test in voltage-clamp mode. *G*: bridge balance adjustment in current clamp mode. *H*: spike detection and rheobase measurement. *I*: standard current injections. *J*: current injection frequency sweep to elicit back-propagating action potentials. *K*: recording during visual stimulus. Gray bars indicate periods where visual stimuli were presented. *L*: membrane test performed during pauses of the visual stimulus for online quality control throughout the recording.

we speculate that additional efforts (e.g., pipette position adjustments, additional suction) taken beforehand could enhance the speed of seal formation or that a different break-in technique would improve yield.

The rate of seal formation is a good indicator of whether the seal will reach 1 GΩ. To determine whether gigasealing was progressing adequately (Fig. 1*vi*), the robot uses a set of time and resistance thresholds. If, after 30, 90, 120, and 180 s after releasing suction, the resistance does not reach a respective threshold of 40, 100, 500, and 1,000 MΩ, the pipette is retracted. This improves overall experimental efficiency by terminating attempts that are unlikely to produce stable recordings.

The algorithm also includes a provision for spontaneous break-in. If the resistance drops below 500 MΩ after previously reaching 1 GΩ, the robot proceeds directly to the electrophysiology recording mode. This approach successfully handled spontaneous break-in events during experiments. The algorithm does not handle cells that break in spontaneously without first having reached 1 GΩ, but these recordings are typically lower quality and would be rejected by the quality control algorithms.

After forming a seal, an experimenter would ideally apply the minimum amount of negative pressure (or voltage) required to break in to avoid damaging the cell or increasing the access resistance. Manually performing break-in using syringes or mouth pipetting techniques requires intensive training and can be error prone.

To break in, we developed an algorithm that ramps the pressure linearly while monitoring seal resistance. Using feedback-control, pressure is abruptly switched off upon break-in. Specifically, pressure is ramped linearly from 0 to −325 mbar over 1.5 s, while monitoring seal resistance using a continuous square wave (10 mV, 100 Hz) voltage injection (Fig. 3*E*). Once break-in occurs (Fig. 3*E*, first arrow), if the resistance drops below 350 MΩ as calculated from the subsequent period of the square wave, the pressure control system halts the pressure ramp. The detection and pressure switch steps require 50 ms (Fig. 3*E*, second arrow) on average from the moment break-in occurs. The pressure decay after detection has a time constant of 38 ms. Thus, the total reaction time of the robot is 50 ms + 57 ms = 107 ms to achieve 95% of atmospheric pressure from the moment break-in occurs. To enable this rapid analog pressure control, we used previously reported electronic pressure control hardware (Kodandaramaiah et al. 2016).

If the membrane fails to rupture after completing the suction ramp, the suction is released, and a second ramp is initiated after a 4-s delay. A voltage zap is delivered (1 V, 25–100 μs) 750 ms into the second

ramp. This combination was always able to either achieve a successful recording or resulted in the loss of the cell.

Electrophysiology software. Following break-in, a membrane test is conducted to assess recording quality (Fig. 3*F*) (Molecular Devices 2006), and the recording is only allowed to continue if the resting membrane voltage is less than −40 mV and if the holding current more than −400 pA to maintain the cell at −65 mV. In addition, throughout the recording, action potentials must overshoot 0 mV and access resistance be <200 MΩ, or else the robot will retract the pipette, replace it, and begin the next trial.

These thresholds are set intentionally low to error on the side of continuing to record rather than accidentally rejecting good cells. For postexperiment, manually performed data analysis, more stringent thresholds were applied. Only recordings with resting membrane voltage less than −55 mV and holding current less than ± 200 pA to maintain the cell at −65 mV were considered successful, consistent with the literature (DeWeese 2007; Gentet et al. 2010; Kim et al. 2014; Kodandaramaiah et al. 2012; Li et al. 2004; Magee and Cook 2000).

The membrane test is followed by a switch to current clamp mode where the bridge balance is adjusted using a 250-pA, 150-Hz square wave (Fig. 3*G*). Figure 3*G* shows the resulting voltage trace after the bridge balance has been adjusted, again automatically, to remove any discontinuities that occur in the voltage trace at the transition between levels of the square wave when the balance is poorly adjusted.

Following a 3-min wait for the recording to stabilize, spikes are elicited by increasing current injections (Fig. 3*H*), in 20-pA increments, and detected using a −10-mV threshold triggered during the injection period. After a spike is detected, the same current amplitude is repeated two additional times to confirm that rheobase current has been reached. If not, it will continue to increase the current. Figure 3*I* shows a standard set of current injections applied to the cell (−1 to 1.5× rheobase divided into 20 levels) to measure the *IV* relationship, h-current, and firing rate versus current injection. To elicit back-propagating action potentials (bAP), a triplet of current pulses (2 ms, amplitude equal to 10 times the rheobase) is injected with frequencies ranging 50–200 Hz in 10-Hz increments (Fig. 3*J*).

Drifting sinusoidal gratings [PsycoPy software, from Peirce (2009)] are then presented (0–335°, 45° orientation resolution, 2-Hz temporal frequency, 2-s duration, 1 s of blank stimulus between presentations, eight replicates, one blank presentation for every 10 sinusoidal presentations, and 10 s blank at the beginning and end of presentation set) (Fig. 3*K*, gray bars) and synchronized to the recording using a photodiode measuring a clock signal displayed on the LCD screens. Every 7 min, the visual stimulation is paused, and a membrane test is performed to check the recording quality and adjust the bridge balance. After completing two replicates of the visual stimulus protocol (35-min total recording duration), the robot retracts the pipette, replaces it, and begins the next trial.

One potential future improvement to this electrophysiology software would be to implement additional current injection repeats for rheobase measurement for cells with high spontaneous firing rates, such as fast-spiking interneurons, which can cause false-positive spike detections and resultantly, underestimate rheobase.

RESULTS

Hardware for Autonomous Serial Patch Clamping

A summary of tasks performed by the robot is shown in Fig. 1. A pipette, after being pulled, must be filled with intracellular solution (Fig. 1*i*), loaded into a pipette holder (Fig. 1*ii*), and positioned accurately over a small craniotomy (Fig. 1,*iii*). Autopatching enables automated steps that localize the pipette into the brain to a region of interest, hunt for a neuron, and form a gigaseal with it, thus enabling the experimenter to break in (Kodandaramaiah et al. 2012) (Fig. 1, *iv-vii*). After the whole cell state is achieved, the patch recording must be tuned (e.g., capacitive compensation, bridge balance) and its quality assessed (e.g., access resistance, holding current) (Fig. 1*viii*), and then the experiment is conducted (e.g., current injections to assess intrinsic properties and sensory stimulus to assess evoked response) (Fig. 1*ix*). Throughout the experiment, the quality should be monitored and the recording terminated if it deviates beyond thresholds or at recording completion (Fig. 1*x*). The pipette must then be retracted and discarded, and the robot must be reset to begin again (Fig. 1*xi*).

The robot shown in Fig. 4 performs all of these steps in a fully automated, autonomous, and consecutive manner. Steps in Fig. 1, *i–iii* are accomplished by a robotic arm (Fig. 4, *i*) that retrieves a pipette from a storage carousel (Fig. 4*ii*), inserts it into a pipette filling station (Fig. 4*iii*), relocates it to a pipette length measurement station to compensate for length variations (Fig. 4*iv*), and inserts it into a pipette holder (Fig. 4*v*) that threads a silver wire electrode into the pipette, forms a pneumatic seal, and precisely aligns the tip of the pipette with the craniotomy. After a recording, pipette retraction and replacement requires 1.5 min. Forty pipettes can be used consecutively. Supplemental Video S1 (https://doi.org/10.6084/m9.figshare.7946504.v2) shows the operation of the robot.

Robotic arm. The robotic arm provides the positional flexibility required to have a modular architecture. It enables hardware to be added, removed, or rearranged within the robot arm's reach making it a generally applicable technique to diverse experimental arrangements. During development, it was discovered that physical separation of the pipette stations and robot arm from the pipette holder minimizes vibrations, drift, thermal effects, and electrical noise from the motors, sensors, and cameras. The pipette handoff performed by the robot arm is essential to achieve low noise and stable recordings.

The arm, which has two rotary joints (Fig. 4*i*), is driven by corresponding stepper motors (NEMA 17, 200 steps/rev) with 99.51:1 planetary gear reduction and photoreflectors for self-calibration and backlash measurement and compensation. The motors are operated open-loop and have a full-step resolution of 140 μm at the end effector. The full extended length of the arm is 457 mm, and it has a working area of 0.54 m^2. The robot arm successfully handled (i.e., picked up, transported, and delivered between all stations) 442/444 pipettes (99.6% reliability).

Pipette storage carousel. For each experiment, 40 pipettes are manually loaded and stored on a motorized carousel (Fig. 4*ii*) for retrieval by the robot arm. The pipette storage carousel features compliant, symmetrical, spring clips to retain and center the pipettes (Fig. 4*ii*, *inset*) and includes a stepper motor and dust cap. A photoreflective sensor is used to calibrate the position of the carousel and provide accurate angular positioning (1.8°/step, 9°/pipette). For each trial, the stepper motor rotates the carousel to present the next pipette to the robot arm with 100% reliability (444/444 pipettes).

Pipette filling station. A pipette filling station (Fig. 4*iii*) threads the pipette over a microfil (Microloader, Eppendorf), while simultaneously applying 5 mbar of pressure to the microfil for 3 s to dispense ~2 μl of intracellular solution. Pipette threading is driven by a stepper motor, lead screw, and linear bearing, translating the pipette 55 mm over the tip of the

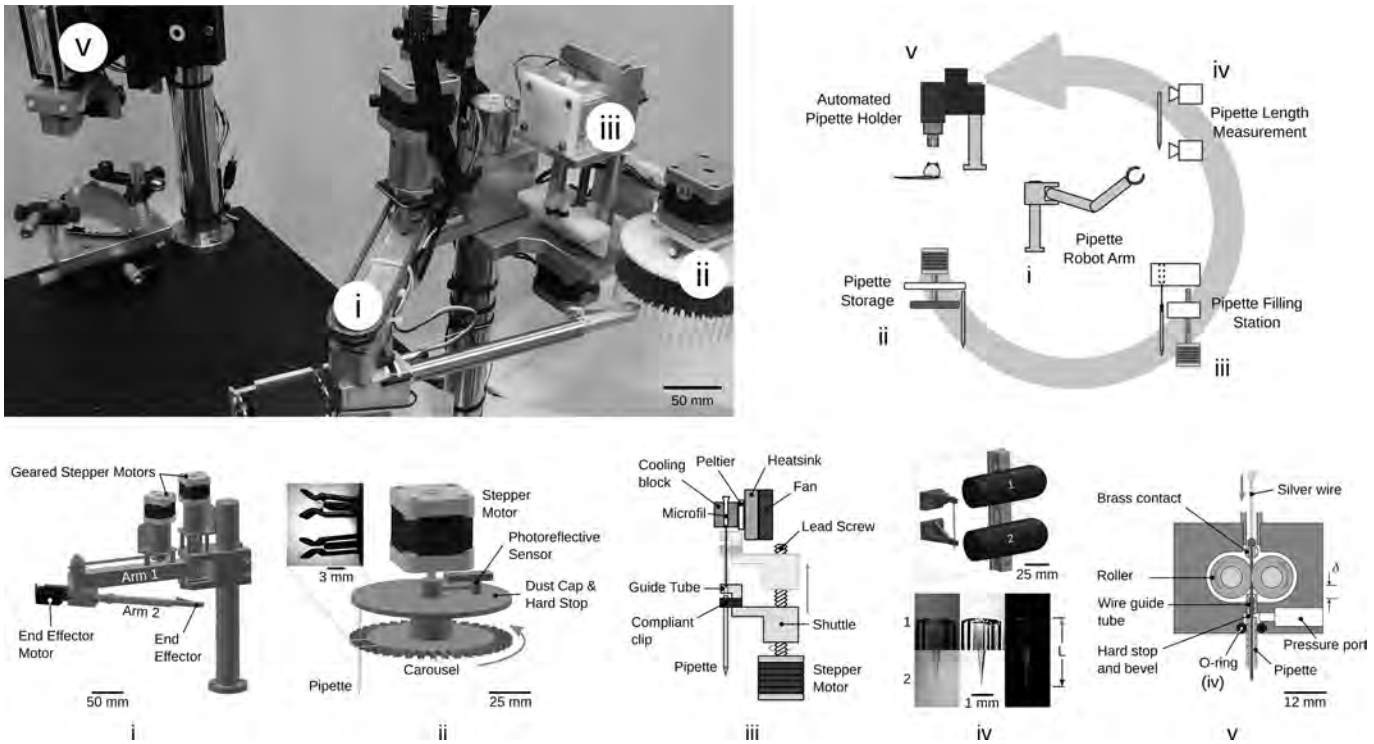

Fig. 4. Photograph (*top left*) and schematics of the autonomous patch clamp robot. *i*: a two degree-of-freedom robot arm moves the pipettes between stations. *ii*: a pipette storage carousel where up to 40 pipettes can be loaded. *iii*: a pipette filling station with thermoelectrically cooled intracellular solution dispenses 3–4 μl. *iv*: a pipette length measurement station accurately measures variation in pipette length for compensation by the automated pipette holder (*v*).

microfil. The tip of the microfil (OD 300 μm) is aligned with the pipette before threading by a guide tube (ID 500 μm). The intracellular solution is maintained at 2°C using a Peltier device to reduce degradation of ATP and GTP (Haynie 2008; Woodbury 2011). Following this initial tip fill, which prevents bubble formation, a higher pressure pulse (1 bar, 100 ms) dispenses the remaining 1–2 μl of fluid directly into the pipette tip. After filling, the pipette is lowered to remove it from the microfil and 8 μl of air is aspirated by the microfil to withdraw the fluid in its tip up into a reservoir maintained at 2°C.

The filling process was successful for 436/442 pipettes (98.6% reliability) during in vivo experimentation. The failures ($n = 6$) were primarily due to user error (e.g., insufficient fluid loaded into microfil) or buckling of the microfil tube during automated threading, preventing the pipette from being filled.

Pipette length measurement. Because pulled pipette lengths can vary by hundreds of micrometers, it is necessary to measure and compensate for length variations so that their tips can be accurately lowered to the specified depth in the brain. Thus, a computer vison system was developed that measures the length of each pipette with 0.9 μm/pixel resolution (Fig. 4*iv*). Two microscopes (Veho, VMS-001, ×225 magnification) acquire images of both ends of the pipette held by compliant clips and apply a sharpening filter, edge detection (Canny), and line detection (Hough) (Fig. 4*iv*) algorithms to measure the length. The standard deviation of repeated measurements of the same pipette was 8 μm, allowing the pipette to theoretically be placed within $\pm$ 24 μm of the targeted depth ($\pm 3\sigma$) when inserted.

Pipette holder. In general, a pipette holder provides *1*) mechanical stiffness, *2*) electrical connectivity, and *3*) pneumatic sealing. An automated pipette holder was developed that performs these functions as well as accurately positions the pipette in the brain. In operation, the automated pipette holder first receives a pipette from the robot arm into a v-groove that provides repeatable kinematic constraint of the pipette above the brain. A linear motor lowers the holder over the pipette held by the robot arm to insert the pipette 4 mm through an o-ring for a pneumatic seal (AS568 size 003, ID 1.42 mm, OD 4.46 mm). A motorized clamp secures the pipette against the v-groove, accurately positioning it. The robot arm then releases the pipette and retracts.

Two silicone rollers (OD 6.25 mm), driven by a small stepper motor, thread a silver wire into the pipette by way of a guide tube (ID 300 μm) and through a brass pin, with 99.5% reliability (434/436 pipettes). Two failures occurred when the end of the silver wire made contact with the flat end of the capillary, causing the wire to buckle as it was pushed by the rollers. Contact with the flat is only possible when the pipette is not inserted into the holder completely.

To reduce noise in the recordings, the entire mechanism was built from nonconductive materials, and the combined length of the silver wire and brass pin was minimized to achieve an open-circuit noise amplitude of 30 pA peak-to-peak. A ball of solder on the end of the wire (OD >500 μm) seats against the brass pin once it is fully threaded to form an electrical connection. Pipette placement reliability was 90.6% (317/350 pipettes) in 200–350-μm craniotomies during in vivo experimentation.

Mechanically, a v-groove in the automated pipette holder constrains the pipette barrel with repeatability of 15.4 μm (standard deviation) in the horizontal plane above the mouse. The tip and barrel of the pipette are not collinear because of a pipette pulling process variation (SD 29.5 μm). Thus, the

root-sum-squared radial repeatability of tip positioning above the craniotomy by the automated pipette holder is 33.2 μm. Additional negligible radial error sources include pipette diameter variation (7-μm SD after binning into 20-μm diameter groups) and elliptical cross-section error (3.5 μm SD).

Thus, we have 99% confidence interval that the true radial positing error is less than 58 μm (χ^2 distribution with measured sample standard deviation of 33.2 μm). From this, we can predict a 99.7% insertion reliability (3σ) for a pipette inserted into a 350-μm craniotomy and 95% reliability (2σ) for 232-μm craniotomies. From the 350/434 pipettes that had good resistance (3–9 M Ohms), experimentally, we measured a 90.6% reliability (317/350 pipettes) in 200–350-μm craniotomies during in vivo experimentation, which closely matches these theoretical results. A failure is defined as a broken pipette tip (measured by impedance change) during insertion.

Pressure control of the pipette holder was performed as previously described (Kodandaramaiah et al. 2016). We further characterized the pneumatic system and found that minimizing the volume of air in the tubing between the pressure control system and pipette is important to reduce response time, although the effect of response time on performance remains unclear.

The automated holder had 0.6 μm/h drift in the axial direction of the pipette and 4 μm/h in the horizontal plane, which was sufficient for achieving stable recordings (an average of 22 min, maximum 110 min)

Software for Autonomous Serial Patch Clamping

For efficiency, modularity, and robustness, we implemented a hybrid state-machine and event-driven architecture, written in C++, that enables multithreaded operation, low latency execution, and segregation between procedural algorithms and hardware-specific functions. To perform a single patch-clamp trial, the autonomous patch clamp robot runs dozens of hardware and software control algorithms, including the autopatcher algorithm (Kodandaramaiah et al. 2012, 2016), as well as several novel algorithms to determine when and how to break into the cell (Fig. 1*vii*), and to perform complete electrophysiological experimental control, Fig. 1, *viii–x* (e.g., online spike detection, rheobase measurement, and recording quality control). Software methods, summarized in Fig. 3, are described in detail in MATERIALS AND METHODS.

In Vivo Performance of Autonomous Patch-Clamp Robot

Experiments reported were conducted as follows. During a 1-mo duration of robot development, ~695 pipettes were used to develop the in vivo algorithms and troubleshoot experimental conditions. During this development phase, six whole cell recordings were obtained. Following this development phase, the full robot was used to measure performance over a 2-mo period. During this performance phase, 444 pipettes were handled in 14 experiments, resulting in 31 whole cell recordings. For results, sections entitled Yield and Throughput, only the results from the performance phase are reported ($n = 31$ recordings). For results, sections entitled Recording Quality, Intrinsic Properties, and Visual Response Characterization, all the recordings from both the performance and development phases are reported ($n = 37$ recordings).

Yield. The overall yield is defined as the percentage of whole cell recordings that meet quality threshold obtained for a given number of pipette insertions. For manual patch-clamp experimentation, yield varies between operators and laboratories (10–50%) (Kodandaramaiah et al. 2012; Koga et al. 2010; Margrie et al. 2002). The autonomous patch-clamp robot described here has a yield of 8.9% (31/350 pipettes). We compare, in Table 1, with previously reported autopatcher yields, since manual experiments do not traditionally note yield of individual steps (e.g., cell detection, gigasealing). The autonomous patch-clamp robot shows a higher incidence of clogged pipettes and cells lost on break-in, and a lower likelihood of obtaining a gigaseal. Potential causes include *1*) the 3–6 h the pipettes were exposed to ambient conditions on the carousel, *2*) the high number of insertions in each of the two craniotomies (12.5 pipettes on average in each) causing tissue damage, and *3*) the lack of manual guidance to finely adjust the location of the tip of the pipette to an optimal location in the craniotomy (undamaged, unused, no vasculature) for each trial. The number of insertions and experiment duration causing low yield aligns with previously reported observations (Kodandaramaiah et al. 2012). These same reasons likely contribute to the higher rate of clogging and reduced rate of gigasealing observed in our results.

Regarding the novel break-in algorithm, we monitor the stability of the gigaseal using thresholds for its magnitude and rate of change (slope). The specific implementation is described in MATERIALS AND METHODS. The break-in algorithm achieved on average 4.4 GΩ seals ($n = 48$ gigaseals out of 198 trials, 24%). All stable recordings (>5 min duration) formed a gigaseal within the first 100 s and stabilized to a value >2 GΩ. The algorithm successfully achieved a whole cell configuration in 65% of break-in attempts (31/48), which is comparable to previous reports of suction pulses (66%) (Desai et al. 2015; DeWeese 2007) and lower than the 82% achieved by the autopatcher alone, which uses pulses of increasing duration although not statistically significantly less (Fisher's Exact test, $P = 0.4$). Manually applied suction ramps were previously

Table 1. *Comparison of success rates for each step between the autopatcher and autonomous autopatcher*

	Autopatcher (Kodandaramaiah et al. 2012)		Autonomous Autopatcher	
		n		*n*
Mice		16		14
Pipettes used				444
Handled successfully			>99%	442/444
Filled			99%	436/442
Wire threaded			>99%	434/436
Pipettes with good resistance (3–9 MΩ)			81%	350/434
Pipettes lowered into the brain		73		350
Unbroken pipettes			91%	317/350
Not clogged	81%		66%	208/317
Cell detected	93%		95%	198/208
Gigaseal	51%		24%	48/198
Whole cell	82%	24	65%	31/48
Yield	33%	24/73	8.9%	31/350

Yield is defined as the percentage of pipettes inserted into the brain that result in a whole cell configuration. Data are populated where available. *n*, Number.

described as having higher success rates than pulses or "fast" ramps (Margrie et al. 2002) indicating that perhaps a ramp duration longer than 1.5 s could improve success rates.

Throughput. The number of recordings per mouse was similar between the autonomous and manned autopatchers with 31 recordings from 14 mice (2.2/mouse) and 24 recordings from 16 mice (1.5/mouse) respectively. The total time for 32 pipettes to be used, on average, was 2.8 h (5.3 min/trial), not including time spent recording.

On average, the robot was loaded with 40 pipettes and used 32 pipettes (40→32) (n = 444 pipettes/14 experiments). One pipette was either mishandled, unfilled, or failed to thread the wire (32→31), and eight (31→23) were outside of the acceptable resistance range (3–9 MΩ) or were otherwise unacceptable (e.g., because of high resistance, variation, or drift) and were automatically replaced by the robot before insertion into the brain. On average, 23 pipettes were inserted into the brain (350 pipettes/14 experiments).

Experiments were typically terminated after 10–15 insertions into each of the two craniotomies within the 4–6 h experimental window.

The pipette throughput is similar for manual autopatching and autonomous autopatching. Manually, 2 min on average are required to prepare a pipette for each patch-clamp trial (Kodandaramaiah et al. 2012), including removal of the pipette from previous trial, filling, threading, and positioning in the craniotomy. The autonomous robot also performs these tasks in ~2 min.

Recording quality. The robot had a 22-min average recording duration (n = 37), with recordings up to 110 min, similar to other reports of in vivo recording stability (20 min (DeWeese 2007), 8–30 min in awake mice (Desai et al. 2015; Margrie et al. 2002), 10–150 min in awake bats (Covey et al. 1996), 57 min on average for anesthetized mice with manual patching (Kodandaramaiah et al. 2012), and 45 min on average in anesthetized mice with autopatching (Kodandaramaiah et al. 2016). A subset of recordings in this work (11/31, 35%) was terminated early after completing the visual stimulus protocol and before the recording quality had degraded below the specified thresholds; thus, the average duration represents a lower bound for the autonomous robot.

Figure 5 shows the recording-quality histograms for whole cell recordings in vivo (n = 37) obtained fully autonomously by the robot. The quality is similar to traditional manual patch clamp recordings in vivo (Kodandaramaiah et al. 2012; Magee and Cook 2000). The recording duration (Fig. 5*A*) does not significantly correlate with the initial pipette resistance, the number of pipette insertions that preceded it, depth, or initial resting membrane potential (correlation coefficients: −0.23, 0.16, 0.004, −0.27, P values: 0.18, 0.35, 0.98, 0.11 respectively).

The average resting membrane potential from all cell types (Fig. 5*B*) with no injected current was −70.1 ± 1.4 mV, indicating good cell health. It is lower than that of the original autopatcher −63.6 ± 2.1 mV (Student's t-test, P = 0.014, means ± SE), largely due to the 4–6.3-mV difference in the Goldman-Hodgkin-Katz potential calculated from the composition of the internal solution, −63.5 mV and −57.2 mV for the solutions used in autonomous and the autopatcher experiments, respectively. For a direct comparison, the holding current required to maintain the cell at −65 mV in current clamp was 38.7 ± 12.7 pA on average compared with the −39.1 ± 22.9 pA for the autopatcher (Student's t-test, P = 0.006). The autonomous autopatcher achieves an average series resistance (Fig. 5*C*) similar to that of the autopatcher, 45 ± 4.2 MΩ and 50 ± 4.8 MΩ, respectively (two-tailed Student's t-test, P = 0.36).

Figure 6 shows the autonomous operation throughout a representative work day. In this 4-h experiment, from a carousel of 40 pipettes, 34 are placed into the brain, resulting in four whole recordings, with an average duration of 23 min. In two separate events denoted in white, an unskilled technician tended to animal welfare, added saline to the craniotomy, or realigned the robot to target a fresh craniotomy on the animal's contralateral side. Recordings 3 and 4 of these were automatically terminated early due to falling below quality control thresholds (resting membrane voltage, high spike threshold, or small AP amplitude) before completing the full visual stimulus presentation.

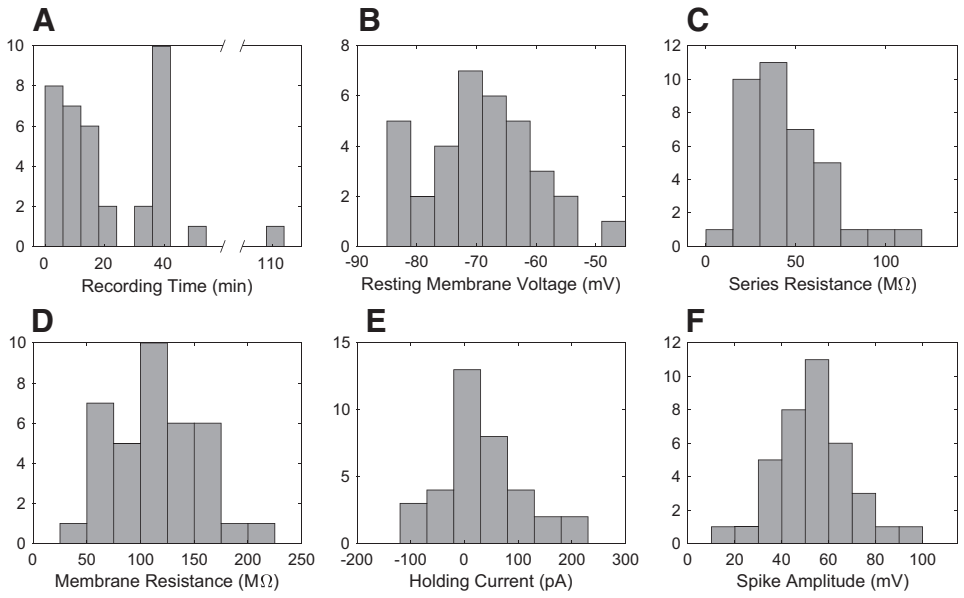

Fig. 5. Histograms of whole cell recording quality, from 37 unmanned robot whole cell recordings: recording time (*A*), resting membrane voltage (*B*), series resistance (*C*), membrane resistance (*D*), holding current (*E*), and spike amplitude (*F*). *E*: note that holding current is defined as the current required to maintain the cell at −65 mV.

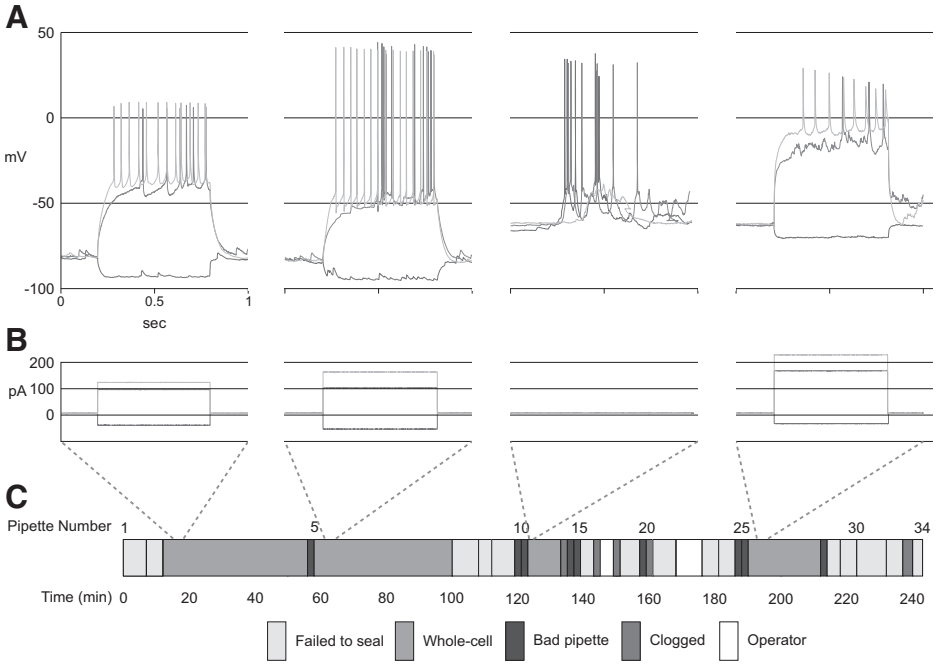

Fig. 6. A representative experiment using the autonomous autopatcher for consecutive patch-clamp recordings in layer 5 of mouse visual cortex in vivo. From 40 loaded pipettes, 34 attempts to record are made in two craniotomies, resulting in four whole cell recordings for visual cortex functional characterization. Operator denotes manual intervention (e.g., switching craniotomy, tending to animal welfare, optimizing anesthesia conditions). *Recordings 3* and *4* were automatically terminated early after they fell below quality thresholds. *A*: current clamp recordings of the four cells recording during this single experiment. *B*: current injection amplitudes and durations corresponding to the recordings in *A*. *C*: timeline of events and duration of the activities during this 4-h experiment.

L5 Cell-Type Classification

Intrinsic properties. On the basis of their intrinsic properties, the 37 recordings were divided into four groups: nonbursting (14 cells), bursting (21 cells), putative somatostatin-positive (SOM+) interneuron (pSOM) (1 cell), and putative parvalbumin-positive (PV+) interneuron (pPV) (1 cell), summarized in Table 2. An entry in the significance column indicates either a P value < 0.05, when comparing two samples with $n > 1$ or if the pSOM or pPV cell is identified as an outlier when compared with the nonbursting and bursting populations (See Supplemental Table S1 at https://doi.org/10.6084/m9.figshare.7946504.v2). Specifically, values more than three median absolute deviations away from the population mean were considered outliers. The average spontaneous firing rate was calculated for cells with recording durations >5 min (NB: $n = 11$, B: $n = 16$, pSOM: $n = 1$, pPV: $n = 1$). The cells classified as nonbursting never exhibited spontaneous interspike intervals <4.9 ms or a firing rate >200 Hz. Bursting cells were identified by minimum interspike intervals <4 ms or firing rates >250 Hz with a minimum of two spikes per burst.

The putative SOM+ interneuron was categorized on the basis of a more depolarized resting voltage, strong h-current (sag), prominent afterhyperpolarization (AHP), and short spike half-width. Although these properties are not exclusive to SOM+ neurons (Berger et al. 2001; Ramaswamy and Markram 2015), this cell exhibited all these traits with the h-current being a dominant differentiator.

The putative PV+ interneuron was categorized on the basis of high-maximum firing rate (500 Hz) and AHP. Figure 7 shows representative responses of each of these cells types to current injection.

Table 2. *Average intrinsic parameters for layer 5 cell types recorded by the autonomous autopatcher*

	Nonbursting	Bursting	Putative SOM Interneuron	Putative PV Interneuron	Statistical Significance
Intrinsic property sample size	$n = 14$	$n = 21$	$n = 1$	$n = 1$	
Depth from pia, μm	556 ± 12.5	532 ± 10.5	562	678	B-pPV
Average resting voltage, mV	−72.2 ± 2.1	−68.5 ± 2.1	−56.5	−61.2	
Slope of membrane sag vs. I_{inj}, mV/pA	−0.002 ± 0.004	−0.013 ± 0.018	0.049	−0.0047	NB-pSOM,B-pSOM
Membrane resistance, MΩ	137 ± 6.73	138 ± 5.86	101	51.7	
Spike threshold, mV	−35.18 ± 2.15	−37.54 ± 1.01	−35.29	−36.78	
Spike half-width, ms	0.76 ± 0.05	0.83 ± 0.03	0.40	0.20	B-pPV
Afterhyperpolarization, mV	8.92 ± 1.49	3.77 ± 0.67	12.70	10.20	NB-B
Recordings >5 min in duration	$n = 11$	$n = 16$	$n = 1$	$n = 1$	
Average spontaneous firing rate, Hz	0.22 ± 0.12	0.94 ± 0.15	0.04	32.5	NB-B,NB-pPV,B-pPV
Visual response sample size	$n = 5$	$n = 9$	$n = 1$	$n = 1$	
Average spike orientation tuning index (1-CirVar)	0.447 ± 0.047	1.00 ± 0.40	0.75	0.27	
Average spike direction tuning index (1-DirCirVar)	0.30 ± 0.09	0.62 ± 0.17	0.93	0.14	

Values are expressed as means ± SE. For the visual response metrics, the subset of cells with sufficient visual stimulus replicates were analyzed ($n = 5$: Nonbursting, $n = 9$: Bursting, $n = 1$: putative SOM+, $n = 1$: putative PV+). Significance column indicates significant difference between cell types shown (P values and test description are listed in Supplemental Table S1 available at https://doi.org/10.6084/m9.figshare.7946504.v2). PV, parvalbumin; SOM, somatostatin.

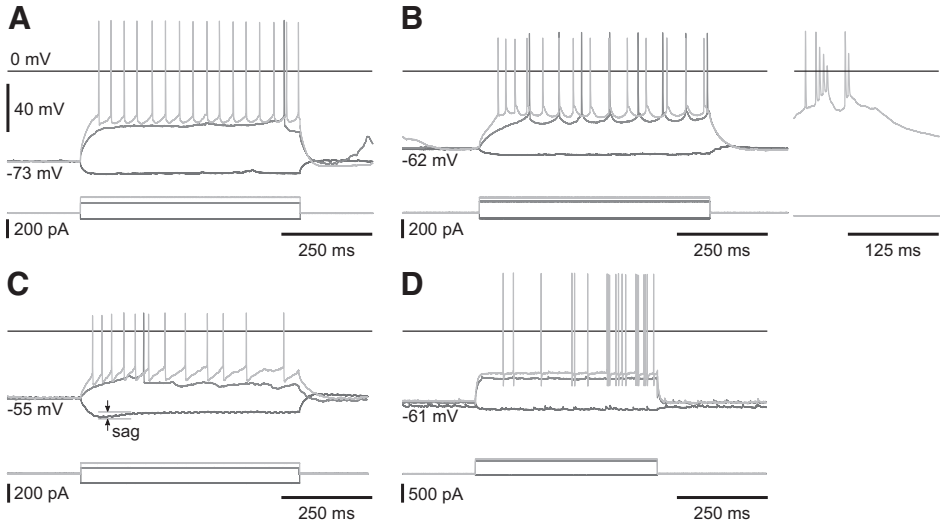

Fig. 7. Representative responses to current injections for all four cell types nonbursting (*A*), bursting (*left*: current injections, *right*: spontaneous burst) (*B*), putative SOM+ interneuron with a strong h-current (sag) (*C*), and putative PV+ interneuron with 0.2-ms spike half-width (*D*).

Intrinsic and Visual Properties of Four Recorded Cell Types

Visual response characterization. Of the 37 recordings, 16 were of sufficient duration for visual response characterization having a minimum of three repeats of each stimulus direction (except for *cell 16*, a putative interneuron, which only had 1–3 repeats for each direction). Representative visually evoked responses from preferred, orthogonal, and antipreferred grating orientations are shown in Fig. 8, along with orientation tuning of visually evoked spiking response of L5 cell types with the preferred direction pointing up.

In our analysis of the visual response, 62.5% ($n = 10/16$) of the cells exhibited a statistically significant spiking response to visual stimuli [rate ratio exact test using a Poisson regression to approximate the rate (Gu et al. 2008)] relative to the level of

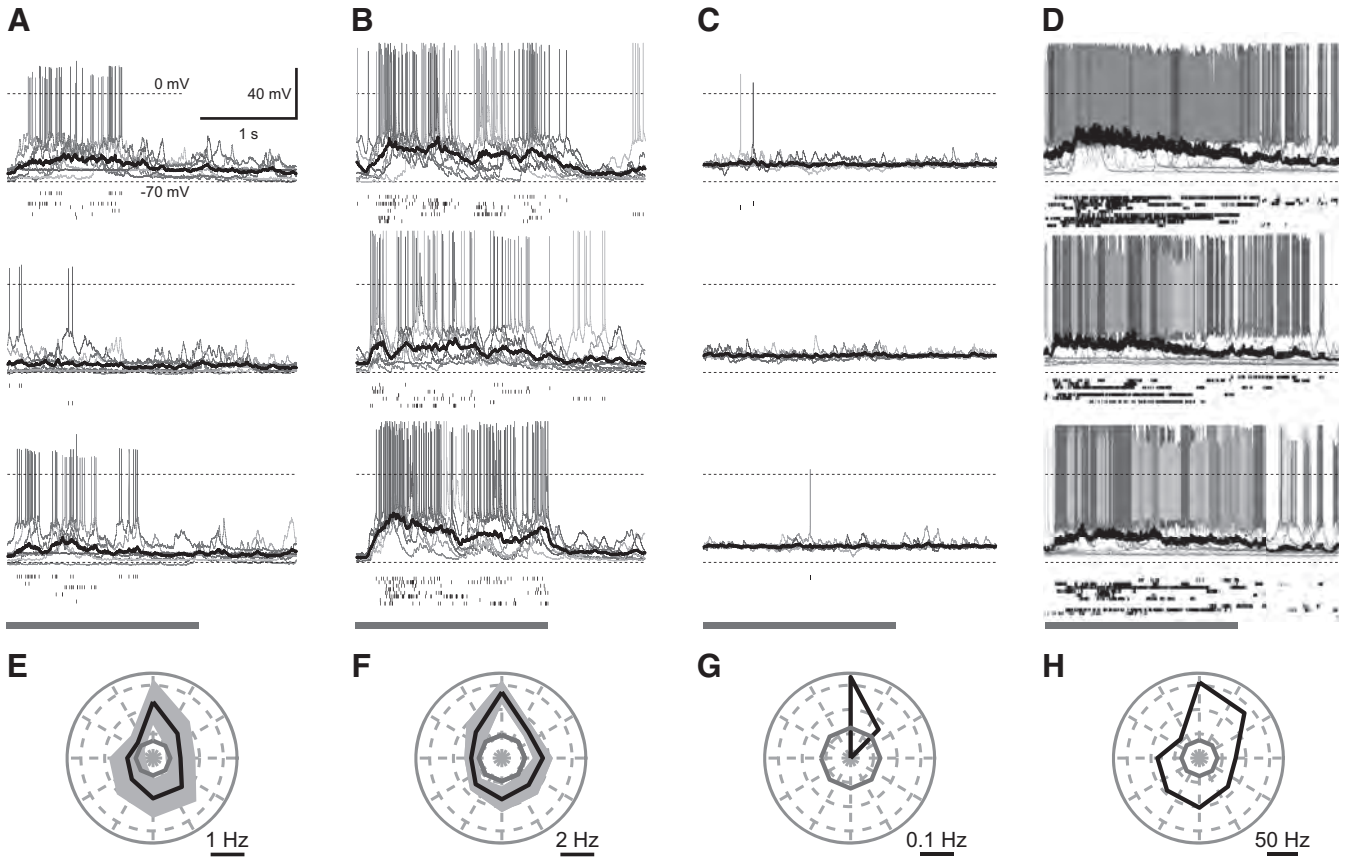

Fig. 8. Visually evoked response (*A–D*) from preferred (*top*), orthogonal (*middle*), and anti-preferred (*bottom*) grating orientations, and spike orientation tuning (*E–H*) of layer 5 cell types with the preferred direction aligned to point up. *A* and *E* are nonbursting, *B* and *F* are bursting, *C* and *G* are putative SOM+, *D* and *H* are putative PV+. *A–D*: gray bar indicates duration of visual stimulation presentation. Solid black line represents the average subthreshold response. Scaling of plots is the same unless otherwise specified. *E–H*: solid black lines indicate the mean spike tuning response and the limits of the black-shaded region represent means ± SE. For *G* and *H*: only 1 cell was recorded so no ± SE is shown. *E–H*: gray solid line indicates the spontaneous background firing rate.

spontaneous spiking activity (see Supplemental Table S2 at https://doi.org/10.6084/m9.figshare.7946504.v2).

The integral of the subthreshold activity during the periods of stimulus and blanking yielded 56.3% (n = 9/16) of cells with a statistically significant response (Student's t-test, see Supplemental Table S2 at https://doi.org/10.6084/m9.figshare.7946504.v2 for P values). This reduced percentage relative to spiking is likely due to the variation introduced by the up and down states that occur during anesthetized recordings. To separate the visual response from this background activity, the integral of the 500 ms of blank prior to and the 500 ms of stimulus after stimulus onset were integrated and compared similar to Rancz et al. (2011). According to this metric, 93.8% (15/16) of cells had significant subthreshold responses to visual stimuli (Student's t-test, see Supplemental Table S3 at https://doi.org/10.6084/m9.figshare.7946504.v2 for P values). Average representative subthreshold responses are shown in Fig. 8, *A–D* (black line). Spikes were removed from the recording before integrating.

Bursting. Spike bursts are thought to be involved in coincidence detection (Shai et al. 2015) and can induce dendritic calcium currents in some cell types, which may play an important role in plasticity by effecting long-term changes in the dendritic arbor and postsynaptic cells (Krahe and Gabbiani 2004). Bursts may enable more reliable signal transmission in certain brain areas (Lisman 1997). Bursting is also thought to be a second "state," possibly enabling multiple signal processing modes within the same cell (Oswald et al. 2004). Lodge et al. show that bursts in dopaminergic neurons (Lodge and Grace 2006) are signs of stimulus salience.

While the traditional definition of bursting cells have firing rates between 100 and 300 Hz (De Kock and Sakmann 2008; Jacob et al. 2012; Shai et al. 2015), we classified cells as bursting by minimum interspike intervals <4 ms or firing rates >250 Hz with a minimum of two spikes per burst. This threshold was chosen because it aligns with the division between cells that exhibit significant depolarization and spike amplitude attenuation during bursting and cells that did not. The distributions of the minimum interspike intervals (ISI) reflect this categorization (mean nonbursting 0.013, mean bursting of 0.003, Student's t-test, and P value of 0.02). While other cells did exhibit high firing rates, some up to ~200 Hz, they did not exhibit depolarization or spike attenuation and were classified as nonbursting. Representative examples are shown in Fig. 9, *A* and *B*.

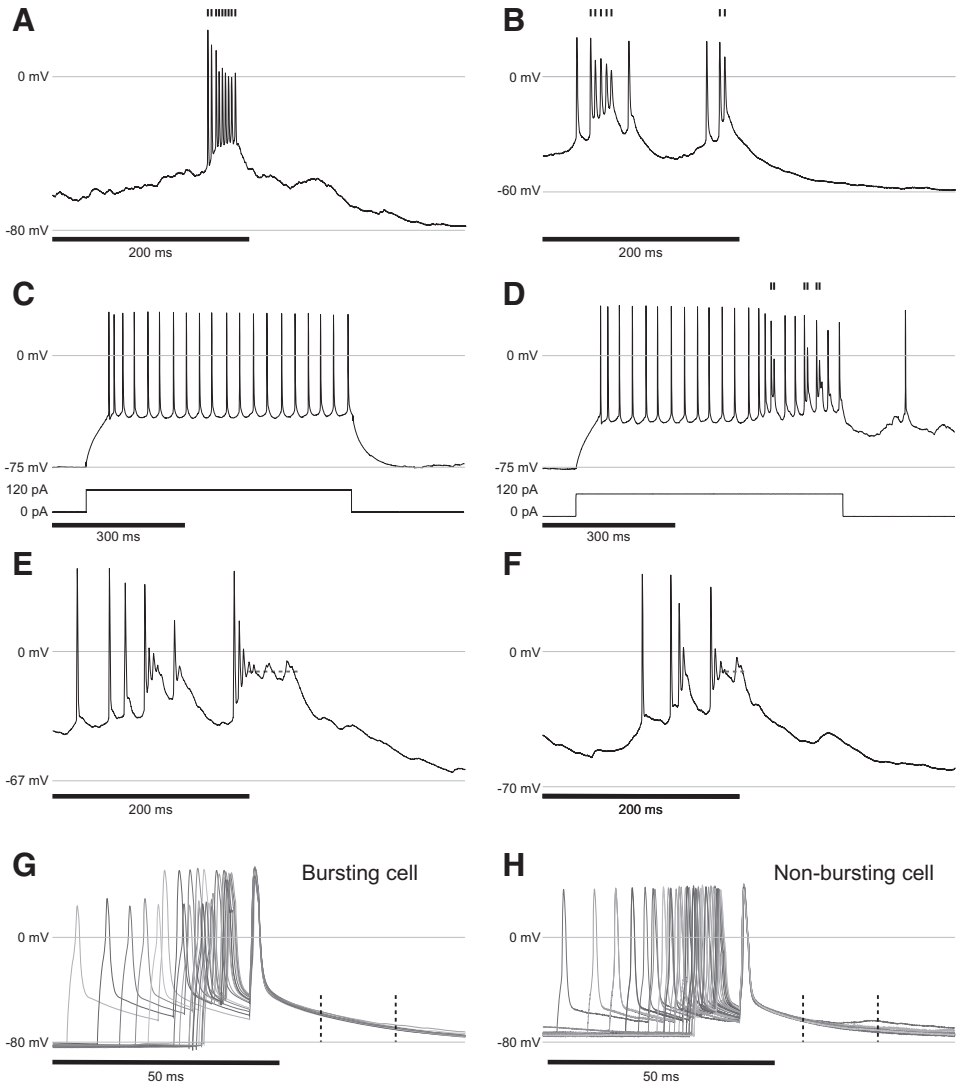

Fig. 9. *A* and *B*: representative bursts from two different cells showing characteristic spike attenuation and depolarization during the burst. *C*: current injection in a bursting neuron showing lack of bursting when injecting 1.5× rheobase. *D*: current injection into the same bursting cell from *C* showing bursting when injection is coincident with spontaneous input to the cell. *A–D*: tic marks signify spikes that are part of a burst. *E* and *F*: representative traces showing plateau potentials (dashed lines) following a burst. *G* and *H*: representative response to three 1.8-ms current pulses (amplitude between 800 and 1000 pA, frequency of pulses increased from 25 to 100 Hz) designed to induce back-propagating action potentials and dendritic calcium currents. Plots are aligned to the last of the three pulses. The epoch between the dashed lines is where depolarization is expected to occur in a subset layer 5 bursting cells when the pulse frequency is above 100 Hz. None of the bursting cells or nonbursting cells in this study exhibited such behavior. In all plots, 0 mV and the resting membrane potential are labeled with gray lines.

For the cells classified as bursting, interspike intervals <0.007 s were considered bursts. Bursts occurred on average at a rate of 3.2 ± 1.4 bursts/min during visual stimulus and 2.1 ± 0.83 bursts/min during blanking on average (two-tailed, Student's *t*-test $P = 0.10$). In our recordings, these rates were too low to correlate with visual stimulus, potentially due to the anesthetized conditions, although one cell did exhibit strong burst direction tuning.

An interesting characteristic of the bursting cells was that they seemed to require spontaneous synaptic input to evoke bursts. In our experiments, somatic current injections were unreliable at evoking bursts despite moderate-amplitude current injections (1.5× rheobase, Fig. 9*C*), differing from reports in L5 of the rat barrel cortex (Helmchen et al. 1999) where somatic current injections elicited bursts and dendritic calcium spikes. Bursts and large postburst polarizations did occur but appear to require the addition of ongoing spontaneous activity (Fig. 9*D*), consistent with the backpropagating and calcium-mediated activity typically seen in V1 L5 cells (Larkum et al. 1999).

In L5 of the rat primary somatosensory cortex, 15% of spikes form part of a burst, making them somewhat rare. For such a salient signal, this certainly seems appropriate, especially considering the added effects of plasticity within the apical tuft due to bAPs and potentiation of downstream targets (De Kock and Sakmann 2008). The patch-clamp technique is currently the only method for observing these behaviors and to determine their functional role in vivo. However, because of the high spontaneous firing rate and low bursting frequency, it will require a large number of recordings to obtain sufficient statistical power (Ascoli et al. 2008; Cadwell et al. 2016) to correlate with function. Because of possible effect of bursting on plasticity, the preferred stimulus may also be better elucidated during awake recordings, while presenting novel visual stimuli. These challenges highlight the need for high-throughput automated recording methods.

Plateau potentials. Plateaus are sustained periods of depolarization above threshold and have been observed in the hippocampus (Epsztein et al. 2011; Fraser and MacVicar 1996; Long and Lee 2012; Suzuki et al. 2008), cerebellum (Llinás and Sugimori 1980), and in pyramidal neurons in L5 (Major et al. 2008) and prefrontal cortex (Milojkovic et al. 2005) of rats. Plateaus in our analysis are defined as a sustained period of depolarization between −5 and −25 mV following an action potential or burst that persists longer than 14 ms. Representative examples are shown in Fig. 9, *E* and *F*.

Plateaus were only observed in bursting cells. Approximately 24% ($n = 5/21$) of bursting cells had at least one spontaneous or visually evoked plateau, and only 9.5% exhibited more than seven plateaus over the 15–30-min recording ($n = 2/21$). The average plateau duration was 30 ± 1.7 ms with a median of 23 ms, and a range between 14 and 128 ms. The average plateau voltage was −14.7 ± 0.17 mV with a median of −14.6 mV, and a range between −7.7 and −18.4 mV. For comparison, place cells in the hippocampus exhibited place-evoked plateaus with an average voltage of −25 mV.

To our knowledge, our experimental results show the first evidence for voltage plateaus in mouse V1 L5. Although a full visual correlation is beyond the scope of this work, the existence of plateaus adds yet another dimension to the already rich behavior set and properties of this layer, including the multiplicity of long-range projections, bursting, and backpropagating APs. It also highlights the need for future intracellular studies, as these features are invisible to extracellular or two-photon interrogation in vivo. Because of the diversity in this layer, the high spontaneous background activity, and the hypothesized role of bursting and plateaus in plasticity yet to be understood, the requisite sample sizes to fully characterize L5 will likely require a high degree of specificity, potentially provided by automated two-photon targeted patch-clamp (Annecchino et al. 2017; Suk et al. 2017), combined with the unmanned, high-throughput operation enabled by this work.

Back-propagating action potentials. bAP were previously characterized in vitro through simultaneous patch-clamp recordings in the soma, apical dendrite, and basal dendrites (Larkum et al. 1999; Nevian et al. 2007; Potez and Larkum 2008; Shai et al. 2015) with one instance of two photon-guided dendritic recordings in vivo. Back-propagating APs are a signature feature of a subset of L5 cells (Shai et al. 2015). For both bursting ($n = 4$) and nonbursting cells ($n = 1$), we did not observe afterdepolarizations (ADP) following bursts, as seen by others in vitro for current pulses with frequencies beyond 100 Hz (Larkum et al. 1999; Potez and Larkum 2008; Shai et al. 2015). Representative examples of this negative result from high-frequency pulse current injections (25–100 Hz) in both cell types are shown in Fig. 9, *G* and *H*.

Because of the challenge of simultaneous dendritic and somatic recordings in vivo, the sensory correlate of this bAP is still unknown. Our results showing the lack of characteristic ADPs align with some reports where dendritic spikes produce no visible ADP at the soma (Larkum et al. 1999) similar to our data. This negative result could be due to our small sample size, or it could indicate that the in vivo extracellular environment or an intact spontaneous inhibitory network activity may suppress this behavior in vivo.

DISCUSSION

We developed a robotic system to autonomously produce multiple consecutive patch-clamp recordings in vivo and demonstrated it by performing visual cortex functional characterization. In the 37 recordings shown, the only steps that were conducted manually were the following: transporting, anesthetizing, and surgically preparing the animal, pulling pipettes, preparing reagents, and craniotomy and animal welfare maintenance during recordings (e.g., saline application, switching to a new craniotomy location, aligning the pipette to the craniotomy, and anesthesia optimization). All other steps—craniotomy (Pak et al. 2015), pipette filling, pipette (re)placement, regional pipette localization, neuron hunting, gigasealing, break-in (Kodandaramaiah et al. 2012), stimulus delivery, and whole cell maintenance and recording—were performed in an autonomous fashion (e.g., Fig. 6). This represents the most fully automated in vivo electrophysiology experiment to date.

Our method does not replace human surgeons and electrophysiologists. To be clear, this approach still requires a human to place the mouse in a stereotaxic device, expose the skull, and align the drill with appropriate structures, perform the durotomy, as well as to pull pipettes and prepare solutions, for example. By automating the most time-consuming and repetitive parts of the experiment, experts can focus on quality surgical preparation, design of experiments, and data analysis.

The robot addresses the three main challenges limiting the acquisition of large data sets of whole cell recordings in vivo: *1*) significant human training and skill required, *2*) human vigilance during 4–6 experiments, and *3*) low probability of obtaining a recording for each inserted pipette (yield).

Between a 6- and 12-mo period of training is typically necessary to begin to acquire high-quality recordings in vivo. Using recent automation (Kodandaramaiah et al. 2016), the autopatcher can reduce this burden by approximately half (3–6 mo). Because the autonomous autopatcher described here does not require training in obtaining and maintaining quality recordings, this burden may be further reduced. We estimate 1 or 2 wk of training would be sufficient to learn to use the autonomous system and gain sufficient aptitude for troubleshooting and performing occasional calibrations (30-min procedure, using a graphical interface). Training in surgical preparation, maintaining animal welfare, pipette fabrication, and solution preparation are still required, yet further automation of these too is possible (Ghanbari et al. 2018; Pak et al. 2015; Stockslager et al. 2016). It is important to note that full autonomy requires that the entire experimental work flow be implemented in software. To adapt the current software for a different workflow would represent a one-time up-front investment, which would be insignificant for large-scale, standardized experimentation, but would be difficult for a laboratory, where experimental work flows change often, and software development resources are lacking. This must be weighed against the increased repeatability, scalability, and predictability of an autonomous system. Vigilance over 4–6 h per recording session is perhaps the most onerous part of in vivo recordings. Repeatedly, an experimenter must prepare each pipette, establish the whole cell configuration, adjust the recording parameters, and conduct the experiment (e.g., apply a sensory stimulus)—all of which are error prone and subjective, and require great skill. This robot significantly reduces the workload and offloads a very complicated experimental protocol to a systematic, deterministic controller, reducing the chance of human error. It enables continuous autonomous operation for up to 40 serial patch-clamp recording trials with minimal operator oversight (e.g., only monitoring the health of the animal and tissue). This approach could enable an expert to oversee multiple parallel experiments, further increasing throughput.

We validated the robot by acquiring 37 high-quality recordings in vivo in a fully automated and systematic manner ($n = 6$ during the development phase; $n = 31$ during performance phase). The quality of the recordings is seen in the average recording duration (22 min), the low average series resistance (45 MΩ), and agreement with published physiological results.

Resting membrane potential, membrane resistance, holding current, and spike amplitude (measured from the spike threshold to the peak) were all within typical ranges for in vivo whole cell recordings. We demonstrated a yield of 8.9% (31/350 pipettes). A typical yield for blind in vivo experiments is between 10 and 50% (Desai et al. 2015; Margrie et al. 2002; Kodandaramaiah et al. 2012). Our demonstrated yield is at the lower end of this range; therefore, yield remains a limiting factor in throughput. We hypothesize that pipette storage in the carousel for several hours rather than freshly pulled pipettes (Hamill et al. 1981) in a close container and suboptimal placement of the pipette tips in craniotomy with respect to vasculature are primary contributors.

L5 Cell-Type Classification and Visual Response Characterization

In 16 of 37 recordings, we report visual response characterization in L5 of V1. Pipettes were lowered to an average depth of 548 μm (range 426–678 μm) from the pia. Of the 16 recordings, two were possible interneurons judging by their intrinsic firing behavior. Approximately 30% of cells in L5 are interneurons (Hattox and Nelson 2007), indicating a possible bias in the robot toward pyramidal cells (only 5%, 2/37, were interneurons), consistent with the autopatcher (Kodandaramaiah et al. 2012) and the patch clamp technique, in general. The putative somatostatin-positive interneuron that we identified (shown in Fig. 7*C* and Fig. 8, *C* and *G*) exhibited a strong h-current and rebound behavior (Lupica et al. 2001; Ma et al. 2006). The intrinsic parameters of this cell also agree well with those identified by others (Cottam et al. 2013; Xu et al. 2013), such as a high resting membrane potential (−56 mV), low spontaneous firing rate (0.05 Hz) (Ma et al. 2010), and short spike half-width. The spike adaptation behavior of this cell is also similar (Ma 2006).

The h-current shown in the cell in Fig. 7*D* and Fig. 8, *D* and *H* is very likely a parvalbumin-positive (PV^+) interneuron due to its high maximum firing rate (~500 Hz) and large AHP) (Hu et al. 2014; McCormick et al. 1985; Rudy and McBain 2001). The PV^+ cells are thought to linearly modulate activity in the visual cortex (Atallah et al. 2012) and are highly visually responsive (79% of all PV^+ cells), as was this cell, with some orientation tuning (Ma et al. 2010). Orientation selectivity index of this cell was 0.53 (1 − circular variance) (Mazurek et al. 2014).

We observed broad tuning of the visual response—somewhat at odds with two-photon calcium imaging data, showing more specific orientation tuning and direction selectivity, probably due to the small sample size, suboptimal spatial frequency tuning (since we only used one frequency), high spontaneous activity, or awake versus anesthetized conditions (Kim et al. 2015).

For comparison, the proportion of visually responsive cells of certain subpopulations in previous studies using two-photon calcium imaging was ~50% for awake mice and 84% for animals under 0.2–0.75% isoflurane [Tlx3-Cre^+, Efr3aCre^+, Glt25d2-Cre^+ (Kim et al. 2015), and CT, CC, CS projection neurons (Lur et al. 2016)]. Our recordings were obtained under 0.75–1.1% isoflurane. Our results showing 10/16 cells (62.5%) that are visually responsive is lower than results obtained from calcium imaging for anesthetized animals (84%). However, the metrics used to determine visually driven cells using two-photon imaging (6%–10% $\Delta F/F$) and patch-clamp recordings (Poisson exact test, including spikes across all stimulus orientations, not just the preferred direction) are not directly comparable considering the different levels of anesthesia and the challenges with indirect measurement of spiking activity using genetically encoded calcium indicators.

With regard to the proportion of visually active cells, the largest sources of error stem from the variation in the proportion of visually active cells depending on the type of indicator used (10–60%; Chen et al. 2013; Kerlin et al. 2010). Calcium

indicators have yet to be fully validated to determine whether they represent the true proportions of population spiking behavior. They do, however, provide large sample sizes for measuring spike orientation, direction, and spatial frequency tuning (1,000s of cells).

The orientation tuning plots agree with previous reports in L5 cells in the auditory cortex showing that bursting cells had a higher spontaneous firing rate than nonbursting neurons, 3.3 Hz and 1.28 Hz, respectively, in an anesthetized preparation using ketamine and xylazine (Suchyna et al. 2009). Similarly, in L5 of the vibrissae pathway under urethane, the thick tufted cells had spontaneous rates of 3.65 Hz and slender tufted cells had a 1.1-Hz rate (De Kock et al. 2007). These morphologies correlate well with IB and RS cells, respectively (Kim et al. 2015; Lur et al. 2016).

Regarding our analysis of voltage plateaus, to our knowledge, our experimental results show the first evidence for voltage plateaus in mouse V1 L5. Although a full visual correlation is beyond the scope of this work, the existence of plateaus adds yet another dimension to the already rich behavior of this layer, including the multiplicity of long-range projection targets, bursting, and back-propagating APs.

Conclusion

This work represents the most fully automated in vivo electrophysiology experiment to date, deploying 40 consecutive pipettes per experiment in an unattended fashion, including functional electrophysiological characterization in vivo. This differs from our previous efforts by replacing the pipette for each attempt, rather than reusing it (Kolb et al. 2016). The state of the art for pipette reuse involves cleaning the electrode tip chemically; however, Kolb et al. (2016) note that pipettes could not be cleaned indefinitely and recommend no more than 10 reuses. Using a new pipette for each trial has certain advantages over reusing pipettes for future applications. Namely, for multiple morphological reconstructions, in situ, unique colored dyes or tags can be used (Steinmeyer and Yanik 2012). Similarly, for mRNA extraction (Cadwell et al. 2016), since each recording attempt uses a fresh pipette, cross-contamination would be avoided, and they can be stored for off-line transcriptomic analysis.

The highly variable and low-yield nature of in vivo patch-clamp recordings will benefit from a standardized, quantitative approach, allowing the development of optimal algorithms and enabling rapid integration with related techniques [e.g., a two-photon guided patch-clamping (Komai et al. 2006; Kitamura et al. 2008), pipette cleaning (Kolb et al. 2016), autopatching (Kodandaramaiah et al. 2012), multipatching (Kodandaramaiah et al. 2018), and two-photon guided autopatching (Annecchino et al. 2017; Suk et al. 2017)].

Specifically, by discretizing and quantifying each step in the process, opportunities to improve yield are revealed. For example, Stoy et al. (2017) have shown that "regional pipette localization" can be improved by avoiding obstacles, such as blood vessels and mitigating clogging (see Table 1), the effect of which is to improve the overall yield of patch clamping. While the autonomous robot lacks the X and Y manipulator to implement this technique, it is a straightforward extension.

A fully automated system will also enable single-cell in vivo pharmacology and high-throughput recordings from precious samples. Conceivably, one experimenter could shepherd an array of robots, supplied with animals by a team of surgeons using automated surgery robots, thus gathering data in a dramatically more high-throughput and systematic fashion, enabling audacious neuroscience goals, such as those of the Allen Institute for Brain Science (Lein et al. 2007; Oh et al. 2014).

ACKNOWLEDGMENTS

We are grateful for the experimental and analysis advice from Annabelle Singer, Nikita Pak, and Tim Jarsky.

GRANTS

This article received the following grant support: NSF Integrative Graduate Education Research Traineeship (0965945), Georgia Institute of Technology Presidential Fellowship, NSF Graduate Research Fellowship, NIH Computational Neuroscience Training grant (DA032466-02), Georgia Tech Neural Engineering Center Seed Grant, NIH grants (NIH R01NS102727, 1-U01-MH106027-01, 1-R01-EY023173, 5-R44-NS083108-03), Georgia Tech Fund for Innovation in Research and Education (GT-FIRE), Georgia Tech Institute for Bioengineering and Biosciences Junior Faculty Award, Georgia Tech Technology Fee Fund, Georgia Tech Invention Studio, George W. Woodruff School of Mechanical Engineering, and the Paul G. Allen and Jody Patton, founders of the Allen Institute for Brain Science.

DISCLOSURES

No conflicts of interest, financial or otherwise, are declared by the authors.

AUTHOR CONTRIBUTIONS

G.H. and B.Y. performed experiments; G.H. and C.R.F. analyzed data; G.H., W.A.S., B.Y., I.K., S.B.K., L.L., U.K., H.Z., B.H., and C.R.F. interpreted results of experiments; G.H. prepared figures; G.H., W.A.S., and C.R.F. drafted manuscript; G.H., W.A.S., and C.R.F. edited and revised manuscript; G.H., W.A.S., I.K., S.B.K., H.Z., B.H., E.S.B., and C.R.F. approved final version of manuscript.

REFERENCES

Annecchino LA, Morris AR, Copeland CS, Agabi OE, Chadderton P, Schultz SR. Robotic automation of in vivo two-photon targeted whole-cell patch-clamp electrophysiology. *Neuron* 95: 1048–1055.e3, 2017. doi:10.1016/j.neuron.2017.08.018.

Ascoli GA, Alonso-Nanclares L, Anderson SA, Barrionuevo G, Benavides-Piccione R, Burkhalter A, Buzsáki G, Cauli B, Defelipe J, Fairén A, Feldmeyer D, Fishell G, Fregnac Y, Freund TF, Gardner D, Gardner EP, Goldberg JH, Helmstaedter M, Hestrin S, Karube F, Kisvárday ZF, Lambolez B, Lewis DA, Marin O, Markram H, Muñoz A, Packer A, Petersen CCH, Rockland KS, Rossier J, Rudy B, Somogyi P, Staiger JF, Tamas G, Thomson AM, Toledo-Rodriguez M, Wang Y, West DC, Yuste R; Petilla Interneuron Nomenclature Group. Petilla terminology: nomenclature of features of GABAergic interneurons of the cerebral cortex. *Nat Rev Neurosci* 9: 557–568, 2008. doi:10.1038/nrn2402.

Atallah BV, Bruns W, Carandini M, Scanziani M. Parvalbumin-expressing interneurons linearly transform cortical responses to visual stimuli. *Neuron* 73: 159–170, 2012. doi:10.1016/j.neuron.2011.12.013.

Berger T, Larkum ME, Lüscher H-R. High I(h) channel density in the distal apical dendrite of layer V pyramidal cells increases bidirectional attenuation of EPSPs. *J Neurophysiol* 85: 855–868, 2001. doi:10.1152/jn.2001.85.2.855.

Bourassa J, Deschênes M. Corticothalamic projections from the primary visual cortex in rats: a single fiber study using biocytin as an anterograde tracer. *Neuroscience* 66: 253–263, 1995. doi:10.1016/0306-4522(95)00009-8.

Cadwell CR, Palasantza A, Jiang X, Berens P, Deng Q, Yilmaz M, Reimer J, Shen S, Bethge M, Tolias KF, Sandberg R, Tolias AS. Electrophysiological, transcriptomic and morphologic profiling of single neurons using Patch-seq. *Nat Biotechnol* 34: 199–203, 2016. doi:10.1038/nbt.3445.

Chen T-W, Wardill TJ, Sun Y, Pulver SR, Renninger SL, Baohan A, Schreiter ER, Kerr RA, Orger MB, Jayaraman V, Looger LL, Svoboda K, Kim DS. Ultrasensitive fluorescent proteins for imaging neuronal activity. *Nature* 499: 295–300, 2013. doi:10.1038/nature12354.

Cottam JCH, Smith SL, Häusser M. Target-specific effects of somatostatin-expressing interneurons on neocortical visual processing. *J Neurosci* 33: 19567–19578, 2013. doi:10.1523/JNEUROSCI.2624-13.2013.

Covey E, Kauer JA, Casseday JH. Whole-cell patch-clamp recording reveals subthreshold sound-evoked postsynaptic currents in the inferior colliculus of awake bats. *J Neurosci* 16: 3009–3018, 1996. doi:10.1523/JNEUROSCI.16-09-03009.1996.

De Kock CPJ, Bruno RM, Spors H, Sakmann B. Layer- and cell-type-specific suprathreshold stimulus representation in rat primary somatosensory cortex. *J Physiol* 581: 139–154, 2007. doi:10.1113/jphysiol.2006.124321.

De Kock CPJ, Sakmann B. High frequency action potential bursts (>or= 100 Hz) in L2/3 and L5B thick tufted neurons in anaesthetized and awake rat primary somatosensory cortex. *J Physiol* 586: 3353–3364, 2008. doi:10.1113/jphysiol.2008.155580.

Desai NS, Siegel JJ, Taylor W, Chitwood RA, Johnston D. MATLAB-based automated patch-clamp system for awake behaving mice. *J Neurophysiol* 114: 1331–1345, 2015. doi:10.1152/jn.00025.2015.

DeWeese MR. Whole-cell recording in vivo. *Curr Protoc Neurosci* Chapter 6: Unit 6.22, 2007. doi:10.1002/0471142301.ns0622s38.

Epsztein J, Brecht M, Lee AK. Intracellular determinants of hippocampal CA1 place and silent cell activity in a novel environment. *Neuron* 70: 109–120, 2011. doi:10.1016/j.neuron.2011.03.006.

Fee MS. Active stabilization of electrodes for intracellular recording in awake behaving animals. *Neuron* 27: 461–468, 2000. doi:10.1016/S0896-6273(00)00057-X.

Fraser DD, MacVicar BA. Cholinergic-dependent plateau potential in hippocampal CA1 pyramidal neurons. *J Neurosci* 16: 4113–4128, 1996. doi:10.1523/JNEUROSCI.16-13-04113.1996.

Gentet LJ, Avermann M, Matyas F, Staiger JF, Petersen CCH. Membrane potential dynamics of GABAergic neurons in the barrel cortex of behaving mice. *Neuron* 65: 422–435, 2010. doi:10.1016/j.neuron.2010.01.006.

Ghanbari L, Rynes M, Hu J, Shulman DS, Johnson G, Laroque M, Shull G, Kodandaramaiah SB. Principles of computer numerical controlled machining applied to cranial microsurgery (Preprint). *bioRxiv* 2018. doi:10.1101/280461.

Gu K, Ng HKT, Tang ML, Schucany WR. Testing the ratio of two poisson rates. *Biom J* 50: 283–298, 2008. doi:10.1002/bimj.200710403.

Hallman LE, Schofield BR, Lin C-S. Dendritic morphology and axon collaterals of corticotectal, corticopontine, and callosal neurons in layer V of primary visual cortex of the hooded rat. *J Comp Neurol* 272: 149–160, 1988. doi:10.1002/cne.902720111.

Hamill OP, Marty A, Neher E, Sakmann B, Sigworth FJ. Improved patch-clamp techniques for high-resolution current recording from cells and cell-free membrane patches. *Pflüg Arch* 391: 85–100, 1981. doi:10.1007/BF00656997.

Hattox AM, Nelson SB. Layer V neurons in mouse cortex projecting to different targets have distinct physiological properties. *J Neurophysiol* 98: 3330–3340, 2007. doi:10.1152/jn.00397.2007.

Haynie DT. *Biological Thermodynamics* (2nd ed.). Cambridge, UK: Cambridge University Press, p. 143, 2008.

Helmchen F, Svoboda K, Denk W, Tank DW. In vivo dendritic calcium dynamics in deep-layer cortical pyramidal neurons. *Nat Neurosci* 2: 989–996, 1999. doi:10.1038/14788.

Hu H, Gan J, Jonas P. Interneurons. Fast-spiking, parvalbumin^{+} GABAergic interneurons: from cellular design to microcircuit function. *Science* 345: 1255263, 2014. doi:10.1126/science.1255263.

Hübener M, Bolz J. Morphology of identified projection neurons in layer 5 of rat visual cortex. *Neurosci Lett* 94: 76–81, 1988. doi:10.1016/0304-3940(88)90273-X.

Hübener M, Schwarz C, Bolz J. Morphological types of projection neurons in layer 5 of cat visual cortex. *J Comp Neurol* 301: 655–674, 1990. doi:10.1002/cne.903010412.

Jacob V, Petreanu L, Wright N, Svoboda K, Fox K. Regular spiking and intrinsic bursting pyramidal cells show orthogonal forms of experience-dependent plasticity in layer V of barrel cortex. *Neuron* 73: 391–404, 2012. doi:10.1016/j.neuron.2011.11.034.

Kasper EM, Larkman AU, Lübke J, Blakemore C. Pyramidal neurons in layer 5 of the rat visual cortex. I. Correlation among cell morphology, intrinsic electrophysiological properties, and axon targets. *J Comp Neurol* 339: 459–474, 1994. doi:10.1002/cne.903390402.

Kerlin AM, Andermann ML, Berezovskii VK, Reid RC. Broadly tuned response properties of diverse inhibitory neuron subtypes in mouse visual cortex. *Neuron* 67: 858–871, 2010. doi:10.1016/j.neuron.2010.08.002.

Kim EJ, Juavinett AL, Kyubwa EM, Jacobs MW, Callaway EM. Three types of cortical layer 5 neurons that differ in brain-wide connectivity and function. *Neuron* 88: 1253–1267, 2015. doi:10.1016/j.neuron.2015.11.002.

Kim J, Matney CJ, Blankenship A, Hestrin S, Brown SP. Layer 6 corticothalamic neurons activate a cortical output layer, layer 5a. *J Neurosci* 34: 9656–9664, 2014. doi:10.1523/JNEUROSCI.1325-14.2014.

Kitamura K, Judkewitz B, Kano M, Denk W, Häusser M. Targeted patch-clamp recordings and single-cell electroporation of unlabeled neurons in vivo. *Nat Methods* 5: 61–67, 2008. doi:10.1038/nmeth1150.

Kodandaramaiah SB, Flores FJ, Holst GL, Singer AC, Han X, Brown EN, Boyden ES, Forest CR. Multi-neuron intracellular recording in vivo via interacting autopatching robots(Abstract). *eLife* 7: e24656, 2018. doi:10.7554/eLife.24656.

Kodandaramaiah SB, Franzesi GT, Chow BY, Boyden ES, Forest CR. Automated whole-cell patch-clamp electrophysiology of neurons in vivo. *Nat Methods* 9: 585–587, 2012. doi:10.1038/nmeth.1993.

Kodandaramaiah SB, Holst GL, Wickersham IR, Singer AC, Franzesi GT, McKinnon ML, Forest CR, Boyden ES. Assembly and operation of the autopatcher for automated intracellular neural recording in vivo. *Nat Protoc* 11: 634–654, 2016. doi:10.1038/nprot.2016.007.

Koga K, Li X, Chen T, Steenland HW, Descalzi G, Zhuo M. In vivo whole-cell patch-clamp recording of sensory synaptic responses of cingulate pyramidal neurons to noxious mechanical stimuli in adult mice. *Mol Pain* 6: 62, 2010. doi:10.1186/1744-8069-6-62.

Kolb I, Stoy WA, Rousseau EB, Moody OA, Jenkins A, Forest CR. Cleaning patch-clamp pipettes for immediate reuse. *Sci Rep* 6: 35001, 2016. doi:10.1038/srep35001.

Komai S, Denk W, Osten P, Brecht M, Margrie TW. Two-photon targeted patching (TPTP) in vivo. *Nat Protoc* 1: 647–652, 2006. doi:10.1038/nprot.2006.100.

Krahe R, Gabbiani F. Burst firing in sensory systems. *Nat Rev Neurosci* 5: 13–23, 2004. doi:10.1038/nrn1296.

Larkum ME, Kaiser KMM, Sakmann B. Calcium electrogenesis in distal apical dendrites of layer 5 pyramidal cells at a critical frequency of back-propagating action potentials. *Proc Natl Acad Sci USA* 96: 14600–14604, 1999. doi:10.1073/pnas.96.25.14600.

Lein ES, Hawrylycz MJ, Ao N, Ayres M, Bensinger A, Bernard A, Boe AF, Boguski MS, Brockway KS, Byrnes EJ, Chen L, Chen L, Chen T-M, Chin MC, Chong J, Crook BE, Czaplinska A, Dang CN, Datta S, Dee NR, Desaki AL, Desta T, Diep E, Dolbeare TA, Donelan MJ, Dong H-W, Dougherty JG, Duncan BJ, Ebbert AJ, Eichele G, Estin LK, Faber C, Facer BA, Fields R, Fischer SR, Fliss TP, Frensley C, Gates SN, Glattfelder KJ, Halverson KR, Hart MR, Hohmann JG, Howell MP, Jeung DP, Johnson RA, Karr PT, Kawal R, Kidney JM, Knapik RH, Kuan CL, Lake JH, Laramee AR, Larsen KD, Lau C, Lemon TA, Liang AJ, Liu Y, Luong LT, Michaels J, Morgan JJ, Morgan RJ, Mortrud MT, Mosqueda NF, Ng LL, Ng R, Orta GJ, Overly CC, Pak TH, Parry SE, Pathak SD, Pearson OC, Puchalski RB, Riley ZL, Rockett HR, Rowland SA, Royall JJ, Ruiz MJ, Sarno NR, Schaffnit K, Shapovalova NV, Sivisay T, Slaughterbeck CR, Smith SC, Smith KA, Smith BI, Sodt AJ, Stewart NN, Stumpf K-R, Sunkin SM, Sutram M, Tam A, Teemer CD, Thaller C, Thompson CL, Varnam LR, Visel A, Whitlock RM, Wohnoutka PE, Wolkey CK, Wong VY, Wood M, Yaylaoglu MB, Young RC, Youngstrom BL, Yuan XF, Zhang B, Zwingman TA, Jones AR. Genome-wide atlas of gene expression in the adult mouse brain. *Nature* 445: 168–176, 2007. doi:10.1038/nature05453.

Li L, Ouellette B, Stoy WA, Garren EJ, Daigle TL, Forest CR, Koch C, Zeng H. A robot for high yield electrophysiology and morphology of single neurons in vivo. *Nat Commun* 8: 15604, 2017. doi:10.1038/ncomms15604.

Li W-C, Soffe SR, Roberts A. A direct comparison of whole cell patch and sharp electrodes by simultaneous recording from single spinal neurons in frog tadpoles. *J Neurophysiol* 92: 380–386, 2004. doi:10.1152/jn.01238.2003.

Lisman JE. Bursts as a unit of neural information: making unreliable synapses reliable. *Trends Neurosci* 20: 38–43, 1997. doi:10.1016/S0166-2236(96)10070-9.

Llinás R, Sugimori M. Electrophysiological properties of in vitro Purkinje cell somata in mammalian cerebellar slices. *J Physiol* 305: 171–195, 1980. doi:10.1113/jphysiol.1980.sp013357.

Lodge DJ, Grace AA. The hippocampus modulates dopamine neuron responsivity by regulating the intensity of phasic neuron activation. *Neuropsychopharmacology* 31: 1356–1361, 2006. doi:10.1038/sj.npp.1300963.

Long MA, Lee AK. Intracellular recording in behaving animals. *Curr Opin Neurobiol* 22: 34–44, 2012. doi:10.1016/j.conb.2011.10.013.

Lupica CR, Bell JA, Hoffman AF, Watson PL. Contribution of the hyperpolarization-activated current (I(h)) to membrane potential and GABA release in hippocampal interneurons. *J Neurophysiol* 86: 261–268, 2001. doi:10.1152/jn.2001.86.1.261.

Lur G, Vinck MA, Tang L, Cardin JA, Higley MJ. Projection-specific visual feature encoding by layer 5 cortical subnetworks. *Cell Rep* 14: 2538–2545, 2016. doi:10.1016/j.celrep.2016.02.050.

Ma WP, Liu BH, Li YT, Huang ZJ, Zhang LI, Tao HW. Visual representations by cortical somatostatin inhibitory neurons—selective but with weak and delayed responses. *J Neurosci* 30: 14371–14379, 2010. doi:10.1523/JNEUROSCI.3248-10.2010.

Ma Y, Hu H, Berrebi AS, Mathers PH, Agmon A. Distinct subtypes of somatostatin-containing neocortical interneurons revealed in transgenic mice. *J Neurosci* 26: 5069–5082, 2006. doi:10.1523/JNEUROSCI.0661-06.2006.

Magee JC, Cook EP. Somatic EPSP amplitude is independent of synapse location in hippocampal pyramidal neurons. *Nat Neurosci* 3: 895–903, 2000. doi:10.1038/78800.

Major G, Polsky A, Denk W, Schiller J, Tank DW. Spatiotemporally graded NMDA spike/plateau potentials in basal dendrites of neocortical pyramidal neurons. *J Neurophysiol* 99: 2584–2601, 2008. doi:10.1152/jn.00011.2008.

Margrie TW, Brecht M, Sakmann B. In vivo, low-resistance, whole-cell recordings from neurons in the anaesthetized and awake mammalian brain. *Pflüg Arch* 444: 491–498, 2002. doi:10.1007/s00424-002-0831-z.

Mazurek M, Kager M, Van Hooser SD. Robust quantification of orientation selectivity and direction selectivity. *Front Neural Circuits* 8: 92, 2014. doi:10.3389/fncir.2014.00092.

McCormick DA, Connors BW, Lighthall JW, Prince DA. Comparative electrophysiology of pyramidal and sparsely spiny stellate neurons of the neocortex. *J Neurophysiol* 54: 782–806, 1985. doi:10.1152/jn.1985.54.4.782.

McElduff F, Cortina-Borja M, Chan S-K, Wade A. When t-tests or Wilcoxon-Mann-Whitney tests won't do. *Adv Physiol Educ* 34: 128–133, 2010. doi:10.1152/advan.00017.2010.

Milojkovic BA, Radojicic MS, Antic SD. A strict correlation between dendritic and somatic plateau depolarizations in the rat prefrontal cortex pyramidal neurons. *J Neurosci* 25: 3940–3951, 2005. doi:10.1523/JNEUROSCI.5314-04.2005.

Molecular Devices. *pClamp 10 User's Guide*. San Jose, CA: Molecular Devices, 2006.

Nevian T, Larkum ME, Polsky A, Schiller J. Properties of basal dendrites of layer 5 pyramidal neurons: a direct patch-clamp recording study. *Nat Neurosci* 10: 206–214, 2007. doi:10.1038/nn1826.

Oh SW, Harris JA, Ng L, Winslow B, Cain N, Mihalas S, Wang Q, Lau C, Kuan L, Henry AM, Mortrud MT, Ouellette B, Nguyen TN, Sorensen SA, Slaughterbeck CR, Wakeman W, Li Y, Feng D, Ho A, Nicholas E, Hirokawa KE, Bohn P, Joines KM, Peng H, Hawrylycz MJ, Phillips JW, Hohmann JG, Wohnoutka P, Gerfen CR, Koch C, Bernard A, Dang C, Jones AR, Zeng H. A mesoscale connectome of the mouse brain. *Nature* 508: 207–214, 2014. doi:10.1038/nature13186.

Oswald A-MM, Chacron MJ, Doiron B, Bastian J, Maler L. Parallel processing of sensory input by bursts and isolated spikes. *J Neurosci* 24: 4351–4362, 2004. doi:10.1523/JNEUROSCI.0459-04.2004.

Pak N, Siegle JH, Kinney JP, Denman DJ, Blanche TJ, Boyden ES. Closed-loop, ultraprecise, automated craniotomies. *J Neurophysiol* 113: 3943–3953, 2015. doi:10.1152/jn.01055.2014.

Peirce JW. Generating stimuli for neuroscience using PsychoPy. *Front Neuroinform* 2: 10, 2009. doi:10.3389/neuro.11.010.2008.

Potez S, Larkum ME. Effect of common anesthetics on dendritic properties in layer 5 neocortical pyramidal neurons. *J Neurophysiol* 99: 1394–1407, 2008. doi:10.1152/jn.01126.2007.

Ramaswamy S, Markram H. Anatomy and physiology of the thick-tufted layer 5 pyramidal neuron. *Front Cell Neurosci* 9: 233, 2015. doi:10.3389/fncel.2015.00233.

Rancz EA, Franks KM, Schwarz MK, Pichler B, Schaefer AT, Margrie TW. Transfection via whole-cell recording in vivo: bridging single-cell physiology, genetics and connectomics. *Nat Neurosci* 14: 527–532, 2011. doi:10.1038/nn.2765.

Rudy B, McBain CJ. Kv3 channels: voltage-gated K+ channels designed for high-frequency repetitive firing. *Trends Neurosci* 24: 517–526, 2001. doi:10.1016/S0166-2236(00)01892-0.

Sakmann B, Neher E. Patch clamp techniques for studying ionic channels in excitable membranes. *Annu Rev Physiol* 46: 455–472, 1984. doi:10.1146/annurev.ph.46.030184.002323.

Shai AS, Anastassiou CA, Larkum ME, Koch C. Physiology of layer 5 pyramidal neurons in mouse primary visual cortex: coincidence detection through bursting. *PLOS Comput Biol* 11: e1004090, 2015. doi:10.1371/journal.pcbi.1004090.

Steinmeyer JD, Yanik MF. High-throughput single-cell manipulation in brain tissue. *PLoS One* 7: e35603, 2012. doi:10.1371/journal.pone.0035603.

Stockslager MA, Capocasale CM, Holst GL, Simon MD, Li Y, McGruder DJ, Rousseau EB, Stoy WA, Sulchek T, Forest CR. Optical method for automated measurement of glass micropipette tip geometry. *Precis Eng* 46: 88–95, 2016. doi:10.1016/j.precisioneng.2016.04.003.

Stoy WA, Kolb I, Holst GL, Liew Y, Pala A, Yang B, Boyden ES, Stanley GB, Forest CR. Robotic navigation to subcortical neural tissue for intracellular electrophysiology in vivo. *J Neurophysiol* 118: 1141–1150, 2017. doi:10.1152/jn.00117.2017.

Suchyna TM, Markin VS, Sachs F. Biophysics and structure of the patch and the gigaseal. *Biophys J* 97: 738–747, 2009. doi:10.1016/j.bpj.2009.05.018.

Suk H-J, van Welie I, Kodandaramaiah SB, Allen B, Forest CR, Boyden ES. Closed-loop real-time imaging enables fully automated cell-targeted patch-clamp neural recording in vivo. *Neuron* 95: 1037–1047.e11, 2017. doi:10.1016/j.neuron.2017.08.011.

Suzuki T, Kodama S, Hoshino C, Izumi T, Miyakawa H. A plateau potential mediated by the activation of extrasynaptic NMDA receptors in rat hippocampal CA1 pyramidal neurons. *Eur J Neurosci* 28: 521–534, 2008. doi:10.1111/j.1460-9568.2008.06324.x.

Tasic B, Yao Z, Smith KA, Graybuck L, Nguyen TN, Bertagnolli D, Goldy J, Garren E, Economo MN, Viswanathan S, Penn O, Bakken T, Menon V, Miller JA, Fong O, Hirokawa KE, Lathia K, Rimorin C, Tieu M, Larsen R, Casper T, Barkan E, Kroll M, Parry S, Shapovalova NV, Hirchstein D, Pendergraft J, Kim TK, Szafer A, Dee N, Groblewski P, Wickersham I, Cetin A, Harris JA, Levi BP, Sunkin SM, Madisen L, Daigle TL, Looger L, Bernard A, Phillips J, Lein E, Hawrylycz M, Svoboda K, Jones AR, Koch C, Zeng H. Shared and distinct transcriptomic cell types across neocortical areas (Preprint). *bioRxiv*, 2017. doi:10.1101/229542.

Tsiola A, Hamzei-Sichani F, Peterlin Z, Yuste R. Quantitative morphologic classification of layer 5 neurons from mouse primary visual cortex. *J Comp Neurol* 461: 415–428, 2003. doi:10.1002/cne.10628.

Vélez-Fort M, Rousseau CV, Niedworok CJ, Wickersham IR, Rancz EA, Brown APY, Strom M, Margrie TW. The stimulus selectivity and connectivity of layer six principal cells reveals cortical microcircuits underlying visual processing. *Neuron* 83: 1431–1443, 2014. [Erratum in *Neuron* 84: 238, 2014.]. doi:10.1016/j.neuron.2014.08.001.

Walz W (Editor). *Patch-Clamp Analysis: Advanced Techniques* **(2nd ed.).** New York: Humana, 2010.

Woodbury CP. *Biochemistry for the Pharmaceutical Sciences*. Burlington, MA: Jones & Bartlett, 2011, p. 211.

Xu H, Jeong H-Y, Tremblay R, Rudy B. Neocortical somatostatin-expressing GABAergic interneurons disinhibit the thalamorecipient layer 4. *Neuron* 77: 155–167, 2013. doi:10.1016/j.neuron.2012.11.004.

Zarrinpar A, Callaway EM. Functional local input to layer 5 pyramidal neurons in the rat visual cortex. *Cereb Cortex* 26: 991–1003, 2016. doi:10.1093/cercor/bhu268.